Heat, Salt, and Freshwater Budgets for a Glacial Fjord in Greenland

REBECCA H. JACKSON AND FIAMMETTA STRANEO

Woods Hole Oceanographic Institution, Woods Hole, Massachusetts

ABSTRACT

In Greenland's glacial fjords, heat and freshwater are exchanged between glaciers and the ocean. Submarine melting of glaciers has been implicated as a potential trigger for recent glacier acceleration, and observations of ocean heat transport are increasingly being used to infer the submarine melt rates. The complete heat, salt, and mass budgets that underlie such methods, however, have been largely neglected. Here, a new framework for exploring glacial fjord budgets is developed. Building on estuarine studies of salt budgets, the heat, salt, and mass transports through the fjord are decomposed, and new equations for calculating freshwater fluxes from submarine meltwater and runoff are presented. This method is applied to moored records from Sermilik Fjord, near the terminus of Helheim Glacier, to evaluate the dominant balances in the fjord budgets and to estimate freshwater fluxes. Throughout the year, two different regimes are found. In the nonsummer months, advective transports are balanced by changes in heat/salt storage within their ability to measure; freshwater fluxes cannot be inferred as a residual. In the summer, a mean exchange flow emerges, consisting of inflowing Atlantic water and outflowing glacially modified water. This exchange transports heat toward the glacier and is primarily balanced by changes in storage and latent heat for melting ice. The total freshwater flux increases over the summer, reaching $1200 \pm 700 \, \mathrm{m^3 \, s^{-1}}$ of runoff and $1500 \pm 500 \, \mathrm{m^3 \, s^{-1}}$ of submarine meltwater from glaciers and icebergs in August. The methods and results highlight important components of fjord budgets, particularly the storage and barotropic terms, that have been not been appropriately considered in previous estimates of submarine melting.

1. Introduction

The Greenland Ice Sheet is currently losing mass, raising global sea levels by 7 mm between 1992 and 2012 (Shepherd et al. 2012). This mass loss is attributed to both surface processes and glacier dynamics at the ice sheet's margins (van den Broeke et al. 2009), with the largest uncertainties in future sea level rise tied to the latter (Lemke et al. 2007). In the past decade, the simultaneous speed-up, thinning, and retreat of many outlet glaciers originated at their marine termini and coincided with ocean warming around Greenland (Howat et al. 2007; Holland et al. 2008). Consequently, submarine melting of these outlet glaciers has been implicated as a driver of dynamic glacier changes (Nick et al. 2009). Our understanding of this submarine melting, however, is hindered by an absence of any direct measurements and a limited understanding of ocean dynamics near the ocean–ice boundary (Straneo and Heimbach 2013).

Submarine melting, along with other freshwater inputs from Greenland, is also critical for unraveling the ice sheet forcing on the ocean. Greenland is a significant and growing source of freshwater to the ocean (Bamber et al. 2012), discharged in the form of submarine melting, runoff, and icebergs. Glacial fjords are the estuaries where liquid freshwater from the ice sheet is mixed and exported into the ocean, yet our understanding of glacial fjord processes is limited in two ways. First, the magnitude and variability of the liquid freshwater fluxes are poorly constrained around Greenland. Estimates of submarine melting have been made with ocean measurements, but they are often derived from simplified models and limited data (e.g., Sutherland and Straneo 2012; Rignot et al. 2010). Runoff into glacial fjords is not directly measured but estimated with regional models and reanalyses that often differ significantly (e.g., Mernild et al. 2010; Andersen et al. 2010; Van As et al.

2014). Second, the glacier-driven circulation from these inputs of freshwater is not well understood. We expect a buoyancy-driven circulation from the freshwater forcing, but, because of the great depth of fjords, this component will often have weak velocities and will be hard to measure. Additionally, glacial fjord dynamics are complicated by a variety of time-dependent flows, like tides and externally forced circulations (Farmer and Freeland 1983; Stigebrandt 2012), that can mask the signal of glacier-driven flow (Jackson et al. 2014).

To improve our understanding of 1) how the ocean impacts glaciers through submarine melting and 2) how glaciers impact the ocean through freshwater forcing, we need better estimates of the heat, salt, and freshwater fluxes in fjords. A growing number of studies attempt to infer submarine melt rates from measurements of ocean heat transport in the fjords where outlet glaciers terminate (Motyka et al. 2003; Rignot et al. 2010; Johnson et al. 2011; Christoffersen et al. 2011; Sutherland and Straneo 2012; Motyka et al. 2013; Xu et al. 2013; Inall et al. 2014; Mortensen et al. 2014; Bendtsen et al. 2015). Water properties and velocity, usually measured over a brief period, are used to estimate ocean heat transport through a fjord cross section. The heat transported toward the glacier is assumed to melt glacial ice, allowing a submarine melt rate to be calculated. Several studies also compute a salt budget to aid in extrapolating or constraining their velocity fields (e.g., Motyka et al. 2003; Rignot et al. 2010). Bartholomaus et al. (2013) employs a variation on this method by calculating meltwater fractions in a fjord and inferring submarine melting from meltwater transport. While several different varieties of this technique have emerged, none includes a discussion of the complete heat, salt, and mass budgets that underlie such estimates. These published estimates are primarily based on snapshots of fjord conditions, and they rely on many implicit or explicit assumptions, some of which we will show are hard to justify generally. Improved equations, along with more comprehensive measurements, are needed to accurately estimate submarine melting and the total freshwater export from the ice sheet.

The unique environment of glacial fjords poses many obstacles to obtaining sufficient data. Many of Greenland's major glaciers have an ice mélange, a thick pack of icebergs and sea ice (Amundson et al. 2010), that renders the near-terminus region inaccessible by boat. Transiting icebergs outside the mélange also impede shipboard and moored observations. As a result, ocean measurements in these fjords are sparse and mostly limited to synoptic surveys (Straneo and Cenedese 2015).

Here, we explore a more thorough formulation of heat, salt, and mass budgets for glacial fjords, and we present an alternative framework for inferring the freshwater inputs from Greenland's glaciers. Building upon the expansive literature on salt budgets in estuaries, we decompose the transport through a fjord cross section and present new equations for calculating meltwater inputs. Our method is applied to 2-yr moored records from Sermilik Fjord, near the terminus of Helheim Glacier, to assess the terms in the heat and salt budgets and to infer freshwater fluxes.

2. Constructing and decomposing fjord budgets

a. Greenlandic glacier–fjord systems

Greenland's glacial fjords share many basic features that distinguish them from the better-studied river estuaries of lower latitudes. Long, narrow, and deep, these fjords connect to the coastal ocean at one end and are bounded by a glacier (or sometimes multiple glaciers) at the other end. The geometry of the glacier termini range from vertical calving fronts to expansive floating tongues (e.g., Stearns and Hamilton 2007; Nick et al. 2012).

Freshwater enters glacial fjords in several ways. Surface melt at the atmospheric boundary of the ice sheet transits through a system of moulins and channels to the base of the glacier and into the fjord at the grounding line, well below the sea surface (Chu 2014). This freshwater is called subglacial discharge or, more generically, runoff. In addition, the glacier discharges freshwater from its terminus in both solid and liquid form as calving icebergs and submarine melting at the ocean–ice interface. Subsequent melting of icebergs can result in an additional liquid meltwater source to the fjord. Unlike typical estuaries, the aforementioned types of liquid freshwater (runoff and submarine melting of glaciers/icebergs) primarily enter the fjord at depth, not at the surface. Additional inputs of freshwater at the surface include terrestrial runoff, precipitation, and sea ice melt.

b. Heat, salt, and mass budgets for a glacial fjord

Here, we construct heat, salt, and mass budgets for a generic glacial fjord. These budgets are the basis for inferring freshwater fluxes from measurements of heat and salt transport. The control volume for the budgets, illustrated in Fig. 1, is the ocean water that is bounded by a fjord cross section at the seaward end, where ocean measurements might be made, and by a glacier at the other end. The other boundaries of the control volume are with the atmosphere at the surface, with icebergs, and with the sidewalls and bottom of the fjord. It is assumed that there is no transfer of heat, salt, or mass through the sidewalls or bottom of the fjord.

For the purpose of this analysis, we group together submarine melting of the glacier and submarine melting of icebergs within the control volume into one meltwater
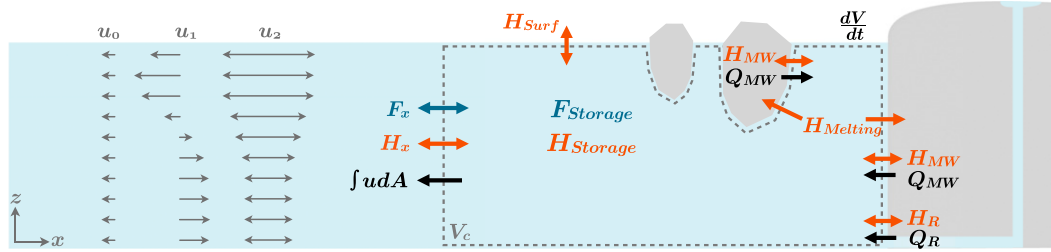
FIG. 1. Schematic of terms in the mass, salt, and heat budgets for a control volume (V_c) shown by the gray dashed rectangle. Note that the control volume does not include the icebergs; it contains only liquid water between the cross section and the glacier. Orange terms are the heat budget, blue terms are the salt budget, and black terms are the mass budget. Iceberg submarine meltwater and glacier submarine meltwater have been combined as Q_{MW}. The left side shows the velocity decomposition ($u = u_0 + u_1 + u_2$) in an idealized case of a two-layer exchange (inflow at depth, outflow at the surface). The mean barotropic velocity u_0 is away from the glacier and balances the mean input of meltwater (Q_{MW}) and runoff (Q_R); u_1 is the mean exchange velocity (time averaged with spatial average removed); and u_2 is the fluctuating velocity (spatial and time average removed).

volume flux Q_{MW}. While iceberg and glacier melting are distinct processes that might have different effects on the ice sheet and ocean, they are indistinguishable in the context of salt, heat, and mass budgets since both meltwater types enter at the seawater freezing point and require latent heat from the ocean to drive melting (e.g., Jenkins 1999). Therefore, any submarine melting that is inferred from the budgets will be the sum of glacial melt and iceberg melt within the control volume. Furthermore, we lump together the terrestrial and subglacial discharge into a single runoff volume flux Q_R, which enters the fjord at a temperature near the freshwater freezing point but does not require latent heat from the ocean to melt. Hence, there are two primary freshwater components that enter the fjord in liquid form: runoff (Q_R) that enters at θ_R, the freezing temperature of freshwater, and meltwater (Q_{MW}) that enters at θ_{MW}, the freezing temperature of seawater in contact with ice. Additionally, evaporation

and precipitation over the surface of the control volume result in a volume flux of Q_{Surf}.

In a mass budget for the liquid water, the volume fluxes of liquid freshwater will be balanced by a volume flux through the cross section (A_x) that bounds the control volume (V_c):

$$\int_{A_x} u \, dA + Q_R + Q_{MW} + Q_{Surf} = \frac{\partial V_c}{\partial t}, \tag{1}$$

where u is the velocity perpendicular to the cross section and $\partial V_c/\partial t$ reflects changes in control volume size from variations in sea surface height, in the concentration of solid icebergs, or in the glacier terminus position. (Using the Boussinesq approximation, variations in density are neglected in the mass budget.) By convention, the velocity and volume fluxes are positive when directed into the control volume (see Table 1 for a list of variables and Fig. 1 for a schematic).

TABLE 1. Relevant variables and budget terms with their meaning and units.

Variables			Terms in heat/salt budgets		
Symbol	Meaning	Units	Symbol	Meaning	Units
ρ	Density of water	kg m^{-3}	H^a	Advective heat flux	J s^{-1}
ρ_{ice}	Density of ice	kg m^{-3}	H^a_x/H_x	Advective heat flux through A_x	J s^{-1}
c_p	Heat capacity of water	J kg^{-1} °C^{-1}	H^a_{MW}/H_{MW}	Advective heat flux from meltwater	J s^{-1}
c_i	Heat capacity of ice	J kg^{-1} °C^{-1}	H^a_R/H_R	Advective heat flux from runoff	J s^{-1}
Q_{MW}	Meltwater volume flux	m^3 s^{-1}	H^a_{Surf}	Advective heat flux from Q_{Surf}	J s^{-1}
Q_R	Runoff volume flux	m^3 s^{-1}	H_{Surf}	Turb./cond./radiative surface heat flux	J s^{-1}
Q_{Surf}	Surface volume flux	m^3 s^{-1}	$H_{Melting}$	Heat used for melting ice	J s^{-1}
θ_{MW}	Temperature of Q_{MW}	°C	$H_{Storage}$	Heat storage in V_c	J s^{-1}
θ_R	Temperature of Q_R	°C	F^a_x/F_x	Advective salt flux through A_x	kg s^{-1}
θ_{Surf}	Temperature of Q_{Surf}	°C	$F_{Storage}$	Salinity storage in V_c	kg s^{-1}
θ_r	Reference temperature	°C			
θ_i	Ice temperature	°C			
L	Latent heat of fusion	J kg^{-1}			
A_x	Cross-section area	m^2			
V_c	Control volume	m^3			

To construct a heat budget for the control volume, it is useful to start with the general form for an ocean heat budget. The heat conservation equation for an incompressible fluid is

$$\underbrace{\rho c_p \oint \theta \mathbf{u} \cdot \mathbf{dA}}_{H^a} = \underbrace{\rho c_p \frac{\partial}{\partial t} \int_{V_c} \theta \, dV}_{H_{\text{Storage}}} + H_f, \qquad (2)$$

where $\mathbf{u} \cdot \mathbf{dA}$ is the inward velocity perpendicular to the boundary, θ is the potential temperature, c_p is the heat capacity of seawater, and ρ is the density of seawater. The heat capacity and density are treated as constants since they vary by less than a few percent. The first term in Eq. (2) is the advective heat flux through all boundaries (H^a); the second term is the change in heat content of the control volume (H_{Storage}); and the third term captures turbulent, conductive, or radiative heat fluxes through the boundaries of the control volume (H_f).

In a glacial fjord, H_f will include surface fluxes and heat used for melting ice: $H_f = H_{\text{Surf}} + H_{\text{Melting}}$. The advective heat fluxes (H^a) through the control volume's boundaries include transport through the fjord cross section (H_x^a) as well as heat transports from runoff, meltwater, and surface mass fluxes ($H_R^a + H_{\text{MW}}^a + H_{\text{Surf}}^a$). We assume that horizontal fluxes through the cross section are resolved by the advective component and thus do not include a horizontal turbulent flux across A_x. Vertical turbulent fluxes can be important in fjords but will not appear in this budget formulation since the control volume is bounded vertically by the free surface and fjord bottom [see Geyer and Ralston (2011) for a review of fjords as strongly stratified estuaries]. The heat budget can thus be written as

$$\underbrace{\rho c_p \int_{A_x} u\theta \, dA}_{H_x^a} + \underbrace{\rho c_p Q_R \theta_R}_{H_R^a} + \underbrace{\rho c_p Q_{\text{MW}} \theta_{\text{MW}}}_{H_{\text{MW}}^a} + \underbrace{\rho c_p Q_{\text{Surf}} \theta_{\text{Surf}}}_{H_{\text{Surf}}^a}$$
$$= \underbrace{\rho c_p \frac{\partial}{\partial t} \int_{V_c} \theta \, dV + H_{\text{Melting}} + H_{\text{Surf}}}_{H_{\text{Storage}}},$$
$$(3)$$

where H_{Melting} and H_{Surf} are positive if the control volume loses heat. There are now four components to the advective heat fluxes on the left side, and these are balanced by changes in heat storage, heat to melt ice, and surface fluxes. The total heat extracted from the ocean to melt ice (H_{Melting}) can be written in terms of the submarine meltwater flux Q_{MW}:

$$H_{\text{Melting}} = \rho Q_{\text{MW}}[L + c_i(\theta_{\text{MW}} - \theta_i)] = \rho Q_{\text{MW}} L_{\text{adj}}, \qquad (4)$$

where L is the latent heat to melt ice, c_i is the heat capacity of ice, θ_i is the ice temperature, and $L_{\text{adj}} = L + c_i(\theta_{\text{MW}} - \theta_i)$ is an adjusted latent heat that takes into account both the heat required to raise ice to the melting temperature and the latent heat to melt ice.

The salt budget is less complex since the runoff, meltwater, and surface mass fluxes do not add or remove salt—they are all mass fluxes of zero salinity. Therefore, the only advective salinity transport will be through the fjord cross section, and this will be balanced by changes in salt storage:

$$\underbrace{\int_{A_x} uS \, dA}_{F_x^a} = \underbrace{\frac{\partial}{\partial t} \int_{V_c} S \, dV}_{F_{\text{Storage}}}. \qquad (5)$$

Equations (1), (3), and (5) are full mass, heat, and salt budgets for a generic glacial fjord. Before proceeding, two more assumptions are made that should hold for many Greenlandic fjords, though not necessarily all. First, the volume flux through the surface of the control volume (Q_{Surf}) and its associated advective heat fluxes (H_{Surf}^a) are both assumed to be negligible. This is based on the assumption that evaporation minus precipitation ($E - P$) over the surface of V_c is small compared to the other mass fluxes. The nonadvective surface heat flux (H_{Surf}) from radiative, latent, and sensible heat fluxes, however, is retained. Second, changes in the size of the control volume ($\partial V_c / \partial t$) from iceberg/glacier variability or sea surface height changes are neglected (see justification in section 5 and appendix A). With these assumptions, the budgets become

$$\text{MASS:} \quad \int_{A_x} u \, dA + Q_R + Q_{\text{MW}} = 0, \qquad (6)$$

$$\text{HEAT:} \quad \underbrace{\rho c_p \int_{A_x} u\theta \, dA}_{H_x^a} + \underbrace{\rho c_p Q_R \theta_R}_{H_R^a} + \underbrace{\rho c_p Q_{\text{MW}} \theta_{\text{MW}}}_{H_{\text{MW}}^a}$$
$$= \underbrace{\rho c_p \int_{V_c} \frac{\partial \theta}{\partial t} \, dV}_{H_{\text{Storage}}} + \underbrace{\rho Q_{\text{MW}} L_{\text{adj}}}_{H_{\text{Melting}}} + H_{\text{Surf}}, \qquad (7)$$

and

$$\text{SALT:} \quad \underbrace{\int_{A_x} uS \, dA}_{F_x^a} = \underbrace{\int_{V_c} \frac{\partial S}{\partial t} \, dV}_{F_{\text{Storage}}}. \qquad (8)$$

The terms from these budgets are illustrated in Fig. 1, with variables defined in Table 1.

c. Time-averaging budgets and decomposing transports

The budgets in Eqs. (6)–(8) are not yet in a practical form to use with observations. First, time averaging is often necessary to separate high-frequency flows from an underlying residual exchange and to reduce the impact of transient changes in heat/salt storage. Second, the barotropic component of the velocity, associated with a net mass transport through the fjord cross section, should be separated from the baroclinic flow to ensure that mass is conserved in the control volume. To address these two issues, the budgets are time averaged over a time scale τ, and the cross-section transports are decomposed in a manner similar to studies of estuarine salt fluxes. Following Lerczak et al. (2006), MacCready and Banas (2011), and others, the along-fjord velocity at the cross section is decomposed into a time and spatially averaged field u_0, a time averaged and spatially varying field u_1, and the time and spatially varying residual u_2:

0. MEAN BAROTROPIC: $u_0(t) = \dfrac{1}{A_x} \overline{\int_{A_x} u \, dA}$,

1. MEAN EXCHANGE: $u_1(y,z,t) = \overline{u(y,z,t)} - u_0(t)$,

2. FLUCTUATING: $u_2(y,z,t) = u(y,z,t) - u_1(y,z,t) - u_0(t)$,

such that $u = u_0 + u_1 + u_2$, and the overbar indicates a temporal running mean over τ (Fig. 1). The same decomposition can be applied to the temperature and salinity fields: θ_0 and S_0 are time and spatially averaged properties, θ_1 and S_1 are time averaged and spatially varying, and θ_2 and S_2 are the residuals.

The decomposition above makes no assumption about the time scale τ. In practice, τ is chosen to distinguish between a mean exchange flow and higher-frequency modes, for example, tides and wind-driven flows. For typical estuarine studies, the averaging time scale τ is between 30 and 50 h, such that u_2 is primarily tides and u_1 captures the subtidal exchange flow. Different time-scale decompositions, however, may be appropriate for different systems, and the averaging time scale τ should be chosen based on the variability in the estuary/fjord. For example, in Sermilik Fjord, shelf-forced flows are the dominant signal in the velocity field, with peak energy at periods of 3–10 days (Jackson et al. 2014), so a τ of several weeks will be required to separate these flows from a residual exchange flow.

Using the decomposed velocity and water properties, the time-averaged fluxes through the cross section have three components:

$$\overline{H^a_x} = \rho c_p \overline{\int_{A_x} (u_0 + u_1 + u_2)(\theta_0 + \theta_1 + \theta_2)\, dA} = \underbrace{\rho c_p u_0 \theta_0 A_x}_{H_0} + \underbrace{\rho c_p \overline{\int_{A_x} u_1 \theta_1 \, dA}}_{H_1} + \underbrace{\rho c_p \overline{\int_{A_x} u_2 \theta_2 \, dA}}_{H_2}$$

$$\overline{F^a_x} = \overline{\int_{A_x} (u_0 + u_1 + u_2)(S_0 + S_1 + S_2)\, dA} = \underbrace{u_0 S_0 A_x}_{F_0} + \underbrace{\overline{\int_{A_x} u_1 S_1 \, dA}}_{F_1} + \underbrace{\overline{\int_{A_x} u_2 S_2 \, dA}}_{F_2} . \tag{9}$$

Six of the cross terms have been dropped because of the averaging properties of the decomposed fields: the spatial average of the mean exchange is zero ($\int_{A_x} u_1 \, dA = 0$, $\int_{A_x} S_1 \, dA = 0$, etc.) and the time average of the fluctuating fields is approximately zero ($\overline{u_2} \approx \overline{S_2} \approx \overline{\theta_2} \approx 0$). The time average of the fluctuating field would be exactly zero if a simple average were performed over the whole record; however, because the overbar denotes a running average (i.e., a low-pass filter), the dropped cross terms are not exactly zero. The errors from dropping these cross terms should generally be small, though their magnitude will depend on the observations (i.e., the time series length and its power spectrum) and the type of low-pass filter used. For the Sermilik Fjord observations,

the small errors from dropping these cross terms are negligible in the budgets (<5% of other terms; Jackson 2016).

In the estuarine literature, F_0 is typically called the river salt flux, F_1 the exchange flux, and F_2 the tidal flux (e.g., MacCready and Geyer 2010). We generalize these terms to "mean barotropic" (F_0, H_0), "mean exchange" (F_1, H_1), and "fluctuating" (F_2, H_2) fluxes, since the freshwater inputs are not from a river, and tides are not necessarily the dominant mode of variability. Note that our definition of mean barotropic is slightly nonstandard because it is a spatial average of the cross section, not just a depth average. Using these decomposed transports, the time-averaged budgets become

$$\text{MASS:} \quad \underbrace{u_0 A_x}_{-\overline{Q}_{\mathrm{FW}}} + \underbrace{\overline{Q}_R + \overline{Q}_{\mathrm{MW}}}_{\overline{Q}_{\mathrm{FW}}} = 0, \tag{10}$$

$$\text{HEAT:} \quad \underbrace{\rho c_p u_0 \theta_0 A_x}_{H_0} + \underbrace{\rho c_p \overline{\int_{A_x} u_1 \theta_1 \, dA}}_{H_1} + \underbrace{\rho c_p \overline{\int_{A_x} u_2 \theta_2 \, dA}}_{H_2} + \underbrace{\rho c_p \overline{Q}_R \theta_R}_{\overline{H}_R} + \underbrace{\rho c_p \overline{Q}_{\mathrm{MW}} \theta_{\mathrm{MW}}}_{\overline{H}_{\mathrm{MW}}}$$

$$= \underbrace{\rho c_p \overline{\int_{V_c} \frac{\partial \theta}{\partial t} \, dV}}_{\overline{H}_{\mathrm{Storage}}} + \underbrace{\rho L_{\mathrm{adj}} \overline{Q}_{\mathrm{MW}}}_{\overline{H}_{\mathrm{Melting}}} + \overline{H}_{\mathrm{Surf}}, \quad \text{and} \tag{11}$$

$$\text{SALT:} \quad \underbrace{u_0 S_0 A_x}_{F_0} + \underbrace{\int_{A_x} u_1 S_1 \, dA}_{F_1} + \underbrace{\int_{A_x} u_2 S_2 \, dA}_{F_2} = \underbrace{\overline{\int_{V_c} \frac{\partial S}{\partial t} \, dV}}_{\overline{F}_{\mathrm{Storage}}}, \tag{12}$$

where $\overline{Q}_{\mathrm{FW}} = \overline{Q}_R + \overline{Q}_{\mathrm{MW}}$ is the total freshwater input and the "a" superscripts denoting "advective" (e.g., $\overline{H}_R^a$) have been dropped.

It is a well-known problem that the heat transports across partial boundaries of a control volume can be dependent on the choice of a reference temperature, while the integrated transport over all boundaries is not (Montgomery 1974). In other words, subtracting a reference temperature from the heat budget does not alter the total budget, though it will change the relative magnitude of certain advective components. When a reference temperature θ_r is subtracted from the heat budget in Eq. (11), it becomes

$$\underbrace{\rho c_p \overline{\int_{A_x} u_2 \theta_2 \, dA}}_{H_2} + \underbrace{\rho c_p \overline{\int_{A_x} u_1 \theta_1 \, dA}}_{H_1} + \underbrace{\rho c_p u_0 (\theta_0 - \theta_r) A_x}_{H_0} + \underbrace{\rho c_p \overline{Q}_R (\theta_R - \theta_r)}_{\overline{H}_R} + \underbrace{\rho c_p \overline{Q}_{\mathrm{MW}} (\theta_{\mathrm{MW}} - \theta_r)}_{\overline{H}_{\mathrm{MW}}}$$

$$= \overline{H}_{\mathrm{Storage}} + \overline{H}_{\mathrm{Melting}} + \overline{H}_{\mathrm{Surf}}. \tag{13}$$

One can see that H_1 and H_2 are independent of the reference temperature, whereas H_0, $\overline{H}_R$, and $\overline{H}_{\mathrm{MW}}$—the terms associated with nonzero mass fluxes—will change their relative magnitudes as a function of the reference temperature. These latter terms can be considered the barotropic heat fluxes across different boundaries: across the fjord cross section in H_0, across the ocean–ice boundaries in $\overline{H}_{\mathrm{MW}}$, and across the openings of runoff channels in $\overline{H}_R$. The three terms in Eq. (13) that are dependent on the reference temperature sum to $\overline{H}_0^{\mathrm{tot}}$, which is independent of the reference temperature:

$$\overline{H}_0^{\mathrm{tot}} = H_0 + \overline{H}_R + \overline{H}_{\mathrm{MW}} = \rho c_p u_0 (\theta_0 - \theta_r) A_x + \rho c_p \overline{Q}_R (\theta_R - \theta_r) + \rho c_p \overline{Q}_{\mathrm{MW}} (\theta_{\mathrm{MW}} - \theta_r)$$

$$= \rho c_p \overline{Q}_R (\theta_R - \theta_0) + \rho c_p \overline{Q}_{\mathrm{MW}} (\theta_{\mathrm{MW}} - \theta_0), \tag{14}$$

where the second line has been rewritten using mass conservation [Eq. (10)]. Variable $\overline{H}_0^{\mathrm{tot}}$ can be called the barotropic heat flux divergence: mass enters the control volume at θ_R and θ_{MW} and leaves, in the barotropic component, at θ_0. Thus, the total heat budget can be rewritten so that each term is now independent of the choice of the reference temperature:

$$H_2 + H_1 + \overline{H}_0^{\mathrm{tot}} = \overline{H}_{\mathrm{Storage}} + \overline{H}_{\mathrm{Surf}} + \overline{H}_{\mathrm{Melting}}. \tag{15}$$

This will be the best form for comparing the magnitude of heat budget components in section 4, such that the results do not depend on the choice of a reference temperature.

d. Estimating freshwater fluxes from observations

Consider the typical case where ocean measurements of velocity, temperature, and salinity are made at a fjord cross section with the goal of inferring submarine melting or runoff. Assuming that neither of the glacial inputs are known a priori, there are three budget equations [Eqs. (10)–(12)] along with (at least) three unknowns: the two freshwater inputs, $\overline{Q}_R$ and $\overline{Q}_{MW}$, and the barotropic velocity u_0.

We consider u_0 to be an unknown because it is too small to be directly measured in almost all fjords. By mass conservation, u_0 is the total freshwater flux $\overline{Q}_{FW}$, divided by the cross-sectional area [Eq. (10)]. In Sermilik, for example, we expect the total freshwater flux $\overline{Q}_{FW}$ to be less than $2000\,\mathrm{m^3\,s^{-1}}$ (see section 4) and the cross-sectional area to be greater than $4.2\,\mathrm{km^2}$, such that $u_0 < 4 \times 10^{-4}\,\mathrm{m\,s^{-1}}$. This is well outside our ability to measure with current technology. Even in a small fjord (e.g., $A_x = 3\,\mathrm{km} \times 100\,\mathrm{m}$) with the same large freshwater flux, the barotropic velocity would still be unmeasurable at $0.006\,\mathrm{m\,s^{-1}}$. This is an important point: the mean barotropic velocity through the cross section is crucial for balancing the mass input of freshwater, but it is not directly measurable. It should, however, be possible to observe the exchange and fluctuating velocity fields, u_1 and u_2, in most fjords.

The heat, salt, and mass budgets can be combined to solve for the three unknowns ($\overline{Q}_R$, $\overline{Q}_{MW}$, and u_0) in terms of quantities that can theoretically be measured (F_1, H_1; F_2, H_2; $F_{Storage}$, $H_{Storage}$; and H_{Surf}). To start, we use the time-averaged salt budget in Eq. (12) to solve for u_0 or $\overline{Q}_{FW}$ in terms of the exchange and fluctuating transports and salt storage:

$$\overline{Q}_{FW} = -u_0 A_x = \frac{1}{S_0}(F_1 + F_2 - \overline{F}_{Storage}). \quad (16)$$

The last two terms on the right-hand side will drop out if the system is in steady state. This is effectively an inversion of the Knudsen relationship (Knudsen 1900; MacCready and Geyer 2010), which is typically used to infer the exchange flow from a salinity profile and known freshwater flux.

In the heat budget of Eq. (11), u_0 can be rewritten in terms of $\overline{Q}_{FW}$ ($-u_0 A_x = \overline{Q}_{FW}$) and $\overline{Q}_R$ in terms of $\overline{Q}_{MW}$ and $\overline{Q}_{FW}$ ($\overline{Q}_R + \overline{Q}_{MW} = \overline{Q}_{FW}$), which allows an expression for $\overline{Q}_{MW}$ in terms of $\overline{Q}_{FW}$ and other measurable components:

$$\overline{Q}_{MW} = \frac{1}{\beta}[\rho c_p \overline{Q}_{FW}(\theta_R - \theta_0) + H_1 + H_2 - \overline{H}_{Storage} - \overline{H}_{Surf}], \quad (17)$$

where $\beta = \rho L_{adj} - \rho c_p(\theta_{MW} - \theta_R)$ and $\overline{Q}_{FW}$ is calculated from Eq. (16). The runoff flux is then the difference between the total freshwater and the meltwater:

$$\overline{Q}_R = \overline{Q}_{FW} - \overline{Q}_{MW}. \quad (18)$$

Thus, in Eqs. (16)–(18), the three budgets have been combined to solve for $\overline{Q}_{FW}$, $\overline{Q}_{MW}$, and $\overline{Q}_R$ in terms of potentially measurable quantities.

We do not explicitly include sea ice in this derivation: sea ice meltwater would be grouped in with Q_{MW} if the ocean supplied the latent heat to melt, whereas it would fall within Q_R if the atmosphere drove melting. (However, there might be a small difference in the adjusted latent heat based on the different initial temperatures of sea ice versus glacial ice.) Sea ice formation would contribute a negative freshwater flux.

Among other things, this decomposition highlights that, in fjords that have significant runoff (likely many Greenlandic fjords in the summer), there is no way to accurately measure submarine melting from a heat budget alone. There are at least two independent unknowns, $\overline{Q}_{MW}$ and $\overline{Q}_R$, in the heat budget [Eq. (11)], which means that this equation alone cannot be used to solve for $\overline{Q}_{MW}$. Another constraint, such as a salt budget, is necessary if runoff is not known a priori. Put another way, volume must be conserved in the control volume: since one cannot measure the net volume fluxes directly, an additional constraint (i.e., the salt budget) is required to ensure volume conservation in the heat budget.

3. Observations from Sermilik Fjord

a. Background on Sermilik Fjord region

Sermilik Fjord is long (90 km), narrow (5–10 km), and deep (>800 m), with no shallow sill to impede exchange with the shelf; the shallowest point in a thalwag between the shelf and glacier is 530 m in the upper fjord (Fig. 2). Helheim Glacier, the fifth-largest outlet of the Greenland Ice Sheet in terms of total ice discharge (Enderlin et al. 2014), drains into the northwest corner of Sermilik Fjord. Two smaller glaciers, Fernis and Midgård, also drain into the fjord in the north and northeast corners. Based on satellite-observed ice velocities and estimated ice thickness, the total ice discharges (iceberg calving plus submarine melting) from Helheim, Midgård, and Fernis are 821 ± 82, 174 ± 32, and $79 \pm 16\,\mathrm{m^3\,s^{-1}}$ water equivalent, respectively, from 1999 to 2008 (Mernild et al. 2010).
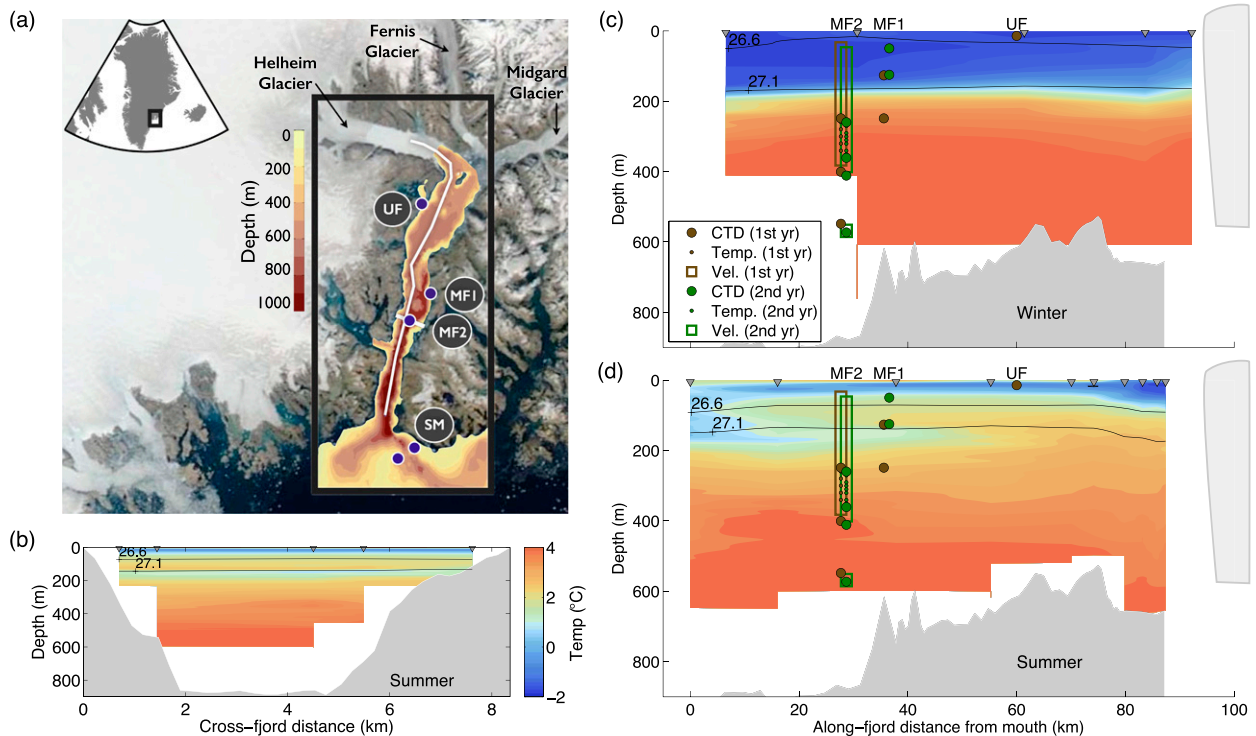
FIG. 2. (a) Satellite image of the Sermilik Fjord region with bathymetry overlaid. Mooring locations and major glaciers are indicated. (b) Cross-fjord section of potential temperature at mooring MF2 location in summer from August 2011 hydrographic survey. (c) Along-fjord section of potential temperature in winter from March 2010 hydrographic survey (Straneo et al. 2011) with depth of instruments from mooring sites MF1, MF2, and UF overlaid. (d)As in (c), but with along-fjord potential temperature of summer conditions from August 2011 hydrographic survey. Isopycnals of $\sigma = [26.6, 27.1]\,\mathrm{kg\,m^{-3}}$ are overlaid in (b)–(d). Triangles at top indicate the CTD station locations used to create temperature section. Locations of cross- and along-fjord sections are shown with white lines in (a).

The water masses found in the fjord are a combination of shelf water masses—Atlantic Water (AW) and Polar Water (PW)—and glacially modified water from submarine meltwater and runoff (Straneo et al. 2011). Because there are at least four different water mass end-members, the meltwater fraction cannot be unambiguously calculated with measurements of temperature and salinity alone (Beaird et al. 2015). One can, however, qualitatively identify regions of glacial modification based on where fjord properties diverge from the shelf water masses.

At the mouth, the fjord connects to an energetic and highly variable shelf region. The southeast shelf of Greenland is subjected to intense alongshore winds, called barrier winds, which occur when low-pressure systems encounter Greenland's steep topography (Harden et al. 2011). Outside of Sermilik, these strong winds are typically from the northeast, which is downwelling-favorable from an oceanographic perspective. The shelf region is characterized by strong oceanic fronts and large variability in water properties, with a series of troughs diverting the East Greenland Coastal Current in close proximity to Sermilik's mouth (Sutherland and Pickart 2008; Harden et al. 2014). Sermilik Fjord is also subjected

to intense, localized along-fjord wind events from downslope flow off the ice sheet (Oltmanns et al. 2014). The fjord is only rarely covered by land-fast sea ice (Andres et al. 2015).

Icebergs are a prominent feature in the fjord—certainly a challenge to obtaining ocean observations and likely a modifier of fjord dynamics. A thick mélange of icebergs extends 10–20 km from the glacier's terminus (Foga et al. 2014), rendering this region inaccessible by boat. The rest of the fjord is littered with transiting icebergs—often moving faster than $0.1\,\mathrm{m\,s^{-1}}$ (Sutherland et al. 2014a) and with keels deeper than 300 m (Andres et al. 2015)—that interfere with shipboard surveys and imperil moorings in the upper water column.

b. Oceanic, wind, and runoff data from Sermilik Fjord

Records of velocity and water properties, shown in Fig. 3, were obtained from two consecutive deployments of midfjord moorings in Sermilik Fjord. (See Fig. 2 and Table 2 for instrument locations and information.) The records span from August 2011 to August 2013, with a 3-month gap during the summer of 2012 when the primary
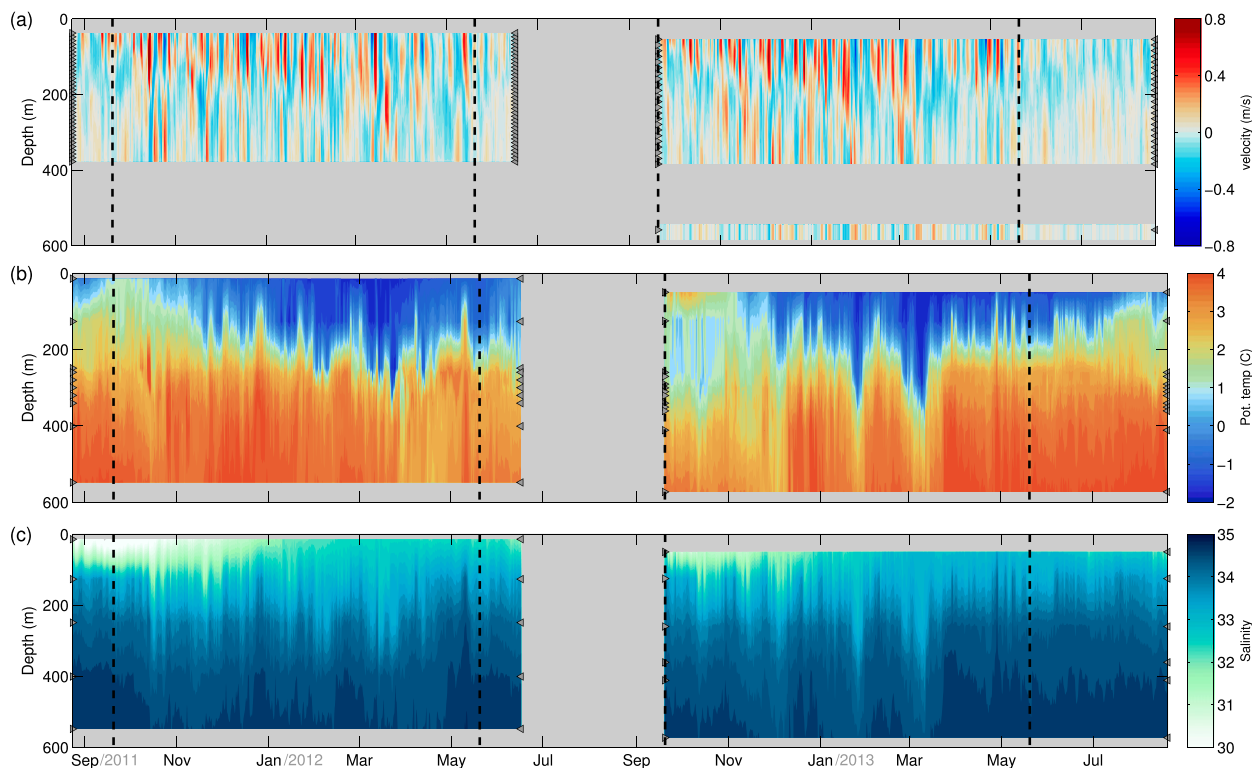
FIG. 3. Two-year records from midfjord moorings MF1 and MF2. (a) Along-fjord velocity, with positive values toward the glacier and negative toward the fjord mouth. (b) Potential temperature. (c) Salinity. Gray triangles indicate the depths of instruments. Vertical dashed black lines at 20 September and 20 May of both years demarcate the summer vs nonsummer regimes.

current profiler failed. Temperature, salinity, and pressure were measured at six depths ranging from 14 to 541 m in 2011–12 and from 50 to 567 m in 2012–13. Temperature was also recorded at six additional depths in each year. An upward-facing, 75-kHz ADCP measured velocity in 10-m bins from 396 m to the surface in the first year and in 15-m bins from 411 m to the surface in the second year. Because of sidelobe contamination from the surface, the bins centered at 27 m and shallower were discarded in the first year, and the bins centered at 39 m and shallower were discarded in the second year. Additionally, a current meter recorded velocity at 567 m for the second year. The water properties were sampled at intervals between 7.5 and 30 min, while the ADCP sampled with 30 ping ensembles at 1- and 2-h intervals in the first and second years, respectively. The velocity measurements have an uncertainty of ± 1 cm s^{-1}.

Two moorings on the shelf (SM in Fig. 2a) recorded temperature, salinity, and pressure at approximately 280 and 300 m for both years (records described in Harden et al. 2014). These time series are only used in θ–S diagrams for context in interpreting fjord water properties. Additionally, synoptic surveys of the fjord and shelf were conducted with XCTDs in March 2010 (Fig. 2c; Straneo et al. 2010) and with lowered CTDs in August 2011 (Figs. 2b,d), September 2012, and August 2013. These

were used to correct drift in the moored CTDs and to provide context for the spatial variability within the fjord.

The water properties from the midfjord moorings are treated as though they were from the same horizontal location, thus neglecting lateral variability between mooring locations and allowing us to create the depth versus time plots in Fig. 3. This assumption is supported by the synoptic surveys of the fjord, which show small lateral variability on the scale of several kilometers compared to variability in depth, time, or lateral variability over the fjord length scale (Jackson et al. 2014). Furthermore, instruments at MF1 (in the middle of the fjord) and MF2 (on the side of the fjord) both recorded properties within 10 m of 260 m depth in 2011–12, and they show nearly identical salinity and temperature records.

The ERA-Interim reanalysis, which has been shown to accurately capture winds on the southeast shelf of Greenland (Harden et al. 2011), is used to assess the seasonality of the shelf wind forcing. Outside of Sermilik Fjord, the velocity component along the principal axis (230° from north) at a point 45 km offshore of the fjord mouth was extracted for an alongshore wind record. Additionally, the Regional Atmospheric Climate Model, version 2.3 (RACMO2.3; Van As et al. 2014; Noel et al. 2015), a high-resolution climate model forced

TABLE 2. List of instruments from midfjord moorings (MF1 and MF2) and upper-fjord moorings (UF1). The 2011 instruments recorded from 23 Aug 2011 to 16 Jun 2012 (or longer for some instruments). The 2012 instruments recorded from 19 Sep 2012 to 19 Aug 2013. Shelf mooring (SM) data, used only for background of θ–S diagrams, is described in Harden et al. (2014).

Mooring	Instrument	Measured properties	Sampling period (min)	Average depth (m)
UF1–2011	SBE 37 MicroCAT CTD	conductivity, temperature, pressure	7.5	14
MF1–2011	SBE 37 MicroCAT CTD	conductivity, temperature, pressure	7.5	125
	SBE 37 MicroCAT CTD	conductivity, temperature, pressure	7.5	261
MF2–2011	RBR XR-420 CTD	conductivity, temperature, pressure	30, 15	246, 657
	Onset HOBO TidbiT v2 Temperature Logger	temperature	30	256, 276, 296, 316, 336, 396
	75 kHz RDI Teledyne Workhorse Long-Ranger ADCP (upward facing)	velocity	120	396 to surface (10 m bins)
	SBE 37 MicroCAT CT(D)	conductivity, temperature, (pressure)	7.5	396, 541
MF1–2012	RBR DR-1050 Depth Recorder	pressure	7.5	50
	SBE 37 MicroCAT CT	conductivity, temperature	7.5	50
	RBR DR-1050 Depth Recorder	pressure	7.5	125
	SBE 37 MicroCAT CT	conductivity, temperature	7.5	125
MF2–2012	75 kHz RDI Teledyne Workhorse Long-Ranger ADCP (upward facing)	velocity	60	411 to surface (15 m bins)
	Onset HOBO TidbiT v2 Temperature Logger	temperature	30	268, 288, 298, 308, 318, 338, 348
	RBR XR-420 CTD	conductivity, temperature, pressure	30	257, 567
	SBE 37 MicroCAT CT(D)	conductivity, temperature, (pressure)	7.5	357, 407
	Nortek AquaDopp Current Meter	velocity	10	567
	RBR DR-1050 Depth Recorder	pressure	10	257

by atmospheric reanalysis, was used to estimate runoff that drains into Sermilik Fjord. Its runoff field provides an estimate of the liquid water that leaves the ice sheet (or terrestrial) surface, but it does not take into account storage or transit within the ice sheet. RACMO2.3 simulations from 1981 to 2013 were used to estimate the runoff flux into the upper half of Sermilik Fjord (i.e., the control volume, or north of our mooring locations) based on the catchment basins in Mernild et al. (2010). The RACMO runoff time series provides context for the seasonality of freshwater fluxes and a point of comparison for our inferred runoff flux. Last, we use bathymetry data from Sutherland et al. (2013) and Schjøth et al. (2012) for Sermilik Fjord and the adjacent shelf region (Fig. 2).

c. Seasonality: Summer versus nonsummer conditions

There is a strong seasonality in fjord conditions that leads us to separate a summer regime (May 20 to September 20) from the nonsummer months (September 20 to May 20), as demarcated by dashed vertical lines in Fig. 3 and subsequent figures. The basic features of the water properties and circulation during the first nonsummer period, September 2011 to May 2012, have been described in Jackson et al. (2014). In that study, it was found that fjord circulation in the nonsummer months is

dominated by a fast ($>0.5\,\mathrm{m\,s^{-1}}$), fluctuating two-layer flow. These pulses originate on the shelf and are driven by fluctuations in the shelf pycnocline. Shelf density fluctuations, in turn, are primarily associated with alongshore shelf winds (Jackson et al. 2014; Harden et al. 2014). The shelf-forced flows (sometimes called the intermediary circulation) drive large volume fluxes into and out of the fjord, causing significant variability in heat content and salinity, due to both heaving of isopycnals and advective property changes within isopycnal layers (Jackson et al. 2014).

In our 2-yr records here, we find that these shelf-forced flows persist throughout both years but are much less energetic during the summer. This coincides with a reduction in wind forcing from the shelf. The alongshore shelf winds have a strong seasonality, with frequent strong events in the nonsummer months and weaker forcing in the summer. A climatology of the ERA-Interim reanalysis wind field shows that alongshore wind strength outside Sermilik peaks in February and reaches a minimum in July (Fig. 4b). During our observational period, the wind seasonality matches that of the climatology, with frequent barrier winds in the nonsummer months and few in the summer. Thus, as one would expect, the amplitude of fjord density fluctuations and resulting shelf-driven circulation are significantly
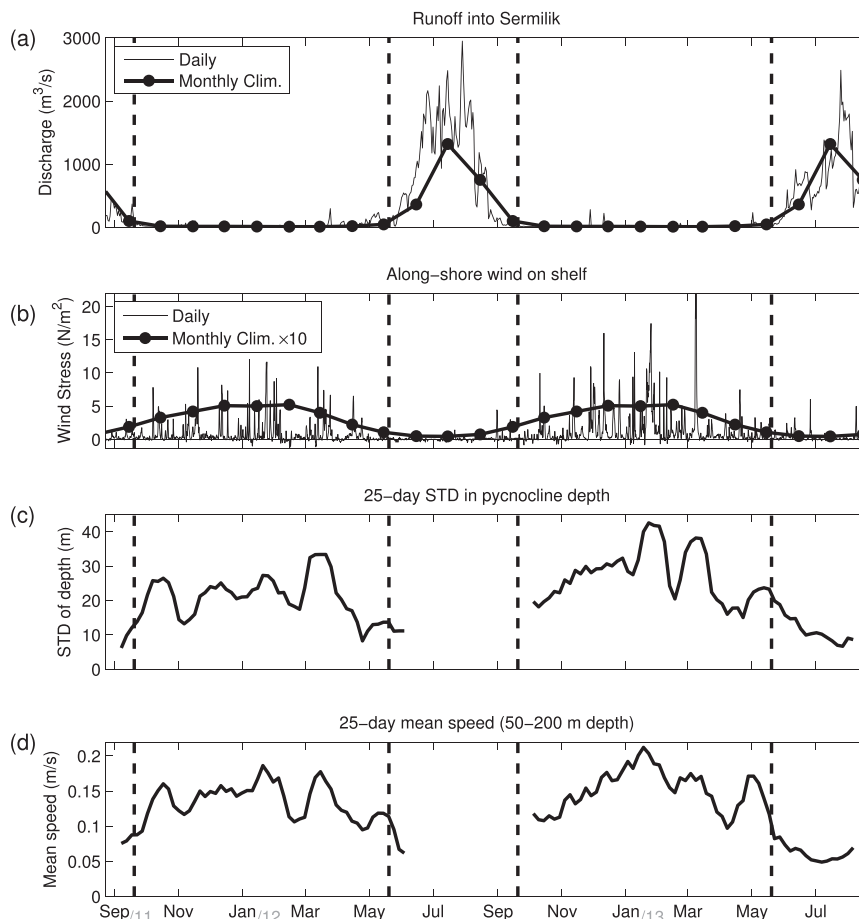
FIG. 4. (a) Runoff from RACMO2.3 into upper Sermilik Fjord for 2011–13 as well as monthly climatology from 1981 to present. (b) Alongshore wind stress on the shelf, 45 km offshore of Sermilik's mouth, for 2011–13 as well as monthly climatology (multiplied by a factor of 10) from 1964 to present. Positive values indicate winds to the southwest, i.e., downwelling favorable. (c) 25-day running standard deviation in the depth of the $\sigma = 26.6 \, \text{kg} \, \text{m}^{-3}$ isopycnal (proxy for variability in fjord pycnocline). (d) 25-day running average speed of 50–200-m depth range (proxy for fjord velocity). Vertical dashed lines separate the summer regime from the nonsummer.

reduced in the summer (Fig. 3). The standard deviation of the pycnocline depth, approximated as the $\sigma = 26.6 \, \text{kg} \, \text{m}^{-3}$ isopycnal, is reduced by 57% in the nonsummer months, while the mean speed is reduced by 59% (Figs. 4c,d).

Direct forcing from along-fjord winds has a similar seasonality, with occasional down-slope events in the nonsummer months and almost none in the summer (Oltmanns et al. 2014). We expect this local wind forcing to drive outflow in the upper layer of the fjord, as suggested in Sutherland et al. (2014a; see also Moffat 2014), though it is difficult to separate this effect from that of the shelf winds in our records, since downslope wind events in Sermilik almost always follow strong alongshore shelf winds.

The buoyancy forcing from glacial inputs is likely, though not proven, to have an opposite seasonality from

the shelf forcing in the Sermilik Fjord region. Surface runoff from the ice sheet will only form when air temperatures are above freezing, which is primarily June–August (e.g., Mernild et al. 2010). RACMO2.3 runoff into Sermilik (Fig. 4a) gives an estimate of melt that leaves the surface of the ice sheet, but it can only provide a rough guide as to when and in what quantity runoff actually enters the fjord. In Fig. 4a, one can see that runoff is close to zero during the nonsummer months, ramps up during June, peaks in July, and decays toward zero in September. These seasonalities in freshwater and shelf forcing lead us to demarcate the summer from the nonsummer months. (The opposing seasonalities in runoff and wind forcing of Sermilik Fjord are not necessarily a general pattern for fjords around Greenland.)
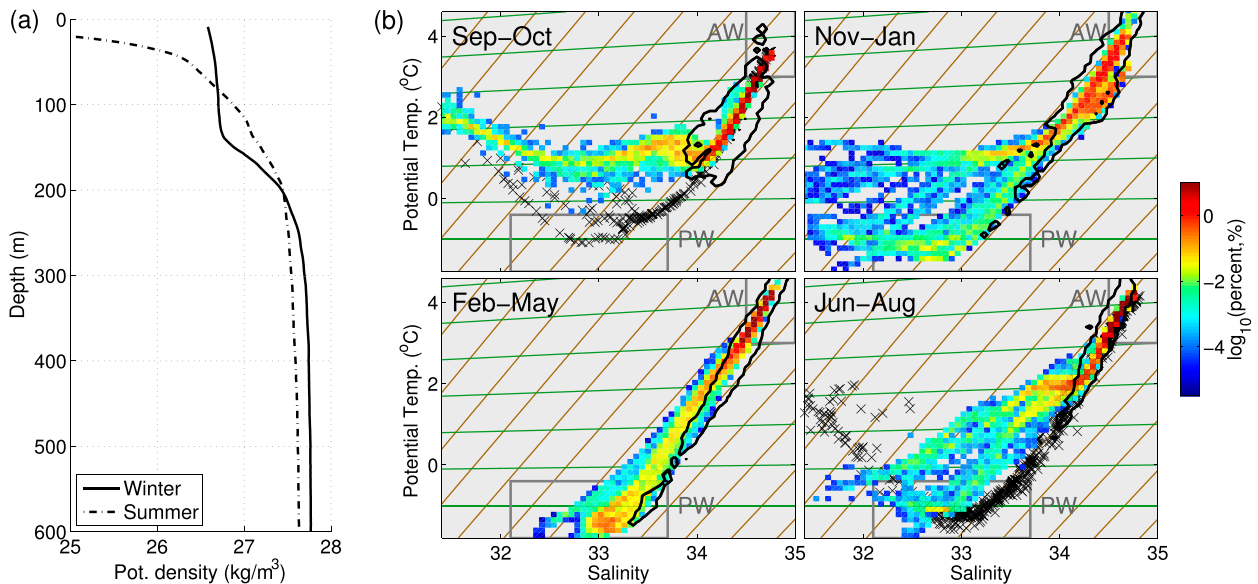
FIG. 5. (a) Average potential density profiles from fjord surveys in summer (August 2011) and winter (March 2010). (b) Potential temperature–salinity diagram of fjord and shelf for the second year (2012–13). Histogram of midfjord properties from data shown in Fig. 3 (using bins of $\Delta S = 0.06$, $\Delta \theta = 0.13°C$) with logarithmic color bar of percent points within each bin. Black contour outlines the shelf properties from CTDs in 280–301-m depth range: the contour traces the bins (also of size $\Delta S = 0.06$, $\Delta \theta = 0.13°C$) that contain more than 0.1% of the shelf points. Black crosses in first and last panel are from CTD surveys of the shelf in September 2012 and August 2013, respectively. Thin brown lines are meltwater mixing lines and thin green lines are runoff mixing lines (see text). Gray boxes outline typical location of AW and PW properties in θ–S space.

Runoff is only one source of freshwater, however, and we can only speculate about the seasonality of the submarine melting. Modeling studies indicate that submarine melting of glaciers increases with subglacial discharge (e.g., Jenkins 2011; Xu et al. 2012; Sciascia et al. 2013; Carroll et al. 2015), which suggests that the seasonality of submarine melting might match that of runoff in the absence of other controls on submarine melting. There are, however, a variety of other factors that could cause different seasonal patterns in submarine melting—for example, the temperature of the AW, the density of the mélange, the fjord's stratification, the presence or absence of PW, the amplitude of shelf-driven circulations and isopycnal heaving, etc.

The observed water properties at the fjord moorings also exhibit a strong seasonality, as previously suggested from hydrographic surveys (Straneo et al. 2011). In the winter, the fjord is largely a two-layer system, with peak stratification between 150 and 250 m (Fig. 5a). During the summer, the fjord is more strongly stratified and the stratification increases toward the surface. Figure 5b shows the seasonal evolution of temperature–salinity (θ–S) diagrams for fjord and shelf properties, with meltwater and runoff mixing lines (see Gade 1979; Straneo et al. 2011) in the background. Throughout the year, AW fills the fjord below ~200 m, and the fjord matches the shelf in this depth range. The upper water

column of the fjord, on the other hand, often differs from the shelf. In the summer and fall months, the fjord waters above ~200 m appear to be modified by mixing with both submarine melting and runoff, suggesting that much of the upper layer is a mixture of deep AW that is upwelled through mixing with glacial freshwater. In the winter and spring, there appears to be no modification due to runoff, and the fjord properties collapse into a tighter θ–S relationship. During this period (February–May in Fig. 5b), fjord properties in the upper layer converge toward the shelf PW properties, with modification due to submarine melting near the middepth pycnocline and perhaps also near the surface.

4. Budgets for Sermilik Fjord

a. Calculating budgets from moored records

Budgets were assessed in Sermilik Fjord for the volume of water upstream of the MF2 mooring site, that is, the northern half of the fjord that receives the discharge from Helheim Glacier and two smaller glaciers, Fernis and Midgård. The moored records at the southern end of the control volume were used to calculate the measurable terms in the heat and salt budgets: the exchange transport (H_1, F_1), the fluctuating transport (H_2, F_2), and the storage ($\overline{H}_{Storage}, \overline{F}_{Storage}$). Although our records are

more comprehensive than previous studies of glacial fjords, particularly in temporal coverage, the spatial coverage of our moorings is still rather limited (Figs. 2, 3).

Budget terms were calculated from the records of velocity, temperature, and salinity from the midfjord moorings that are separated by several kilometers (MF1 and MF2 in Fig. 2, Table 2), where the lateral variability between these moorings has been neglected (see section 3b). We grid the velocity and water properties in depth and time to match the ADCP bins: for the first year, 10 m in depth and 1 h in time, and for the second year, 15 m in depth and 2 h in time.

To calculate the exchange, fluctuating, and storage terms, the velocity and water properties were extrapolated at each time step so that they spanned from the surface to 800 m depth. The velocity records were extrapolated with four different methods: 1) extrapolation to the surface assuming a constant value equal to the top ADCP bin, then extrapolation to the bottom with a constant value that gives zero mass flux; 2) extrapolation to the surface assuming a constant shear equal to the average shear over the top three ADCP bins, then extrapolation to the bottom with a constant value that gives zero mass flux; 3) extrapolation at the bottom assuming a constant value equal to the deepest ADCP bin, then extrapolation at the surface with a constant value that gives zero mass flux; and 4) extrapolation at the bottom assuming zero velocity at 800 m and linear shear between 800 m and the deepest ADCP bin, then extrapolation at the surface with a constant value that gives zero mass flux. In all of these cases, zero mass flux is defined as

$$\int_H^0 u_{ex}(z,t)W(z)\,dz = 0,$$

where $H = 800$ m, u_{ex} is the extrapolated velocity field, and $W(z)$ is the width of the fjord as a function of depth at the MF2 mooring site. Figure 2b shows bathymetry at the fjord cross section; the width varies from approximately 8 km at the surface to 3 km at 800 m depth. We extrapolate to require zero mass flux so that the extrapolated velocity is essentially a purely baroclinic field. As discussed in section 2, there must be a mean outflowing barotropic velocity u_0 to balance the inputs of

freshwater, but it is too small to measure with an ADCP ($\ll 1$ cm s^{-1}). Thus, we do not assume that there is zero mass flux: u_0 is an unknown and nonzero. Instead, we assume that our measured extrapolated velocity is an estimate of the baroclinic fields ($u_1 + u_2$) such that $u(z,t) = u_0(t) + u_{ex}(z,t)$.

The temperature and salinity records were extrapolated to 800 m depth by assuming a constant value equal to the deepest CTD. This is supported by the very weak stratification observed below 500 m [see profiles in Fig. 5a and moored records in Jackson et al. (2014)]. Water properties were extrapolated to the surface by assuming 1) a constant value equal to the top CTD and 2) a constant gradient based on the top two CTD observations. A comparison with the shipboard surveys of the fjord suggests that this spread of extrapolations does well at capturing the surface conditions in the winter, when there is a deep mixed layer, but it might overestimate the salinity of the top 10 m in the summer when stratification increases toward the surface (Fig. 5a).

The spread from these various extrapolation techniques was included as part of the estimated uncertainty in our calculations. Each version of the velocity field (four versions) was combined with each version of the water properties (two versions) to calculate the budget terms and freshwater fluxes in eight different ways. The total spread from these results is included in all subsequent error bars (e.g., Figs. 7, 8) and uncertainties.

There is a 530-m-deep sill in the upper fjord between the mooring site and the glacier (Fig. 2), which suggests that the water below 530 m at the mooring site could be largely isolated from heat, salt, and mass exchanges with the glacier. We performed the extrapolations and budget calculations for the water column above 530 m, but the results were similar and are not sensitive to the depth of extrapolation.

To decompose the velocity, temperature, and salinity fields, we neglected cross-fjord variability and use the depth-variable fjord width (Fig. 2). Because we have extrapolated the velocity field to require zero mass flux, there is no need to remove the barotropic velocity when calculating u_1 and u_2 from the observed velocity field u_{ex}. Accordingly, the decomposed fields are

$$u_0(t) = \text{unknown}, \quad u_1(z,t) = \overline{u_{ex}(z,t)}, \quad u_2(z,t) = u_{ex}(z,t) - u_1(z,t)$$

$$\theta_0(t) = \frac{1}{H}\int_H^0 \overline{\theta_{ex}(z,t)}W(z)\,dz, \quad \theta_1(z,t) = \overline{\theta_{ex}(z,t)} - \theta_0(t), \quad \theta_2(z,t) = \theta_{ex}(z,t) - \theta_1(z,t) - \theta_0(t)$$

$$S_0(t) = \frac{1}{H}\int_H^0 \overline{S_{ex}(z,t)}W(z)\,dz, \quad S_1(z,t) = \overline{S_{ex}(z,t)} - S_0(t), \quad S_2(z,t) = S_{ex}(z,t) - S_1(z,t) - S_0(t),$$
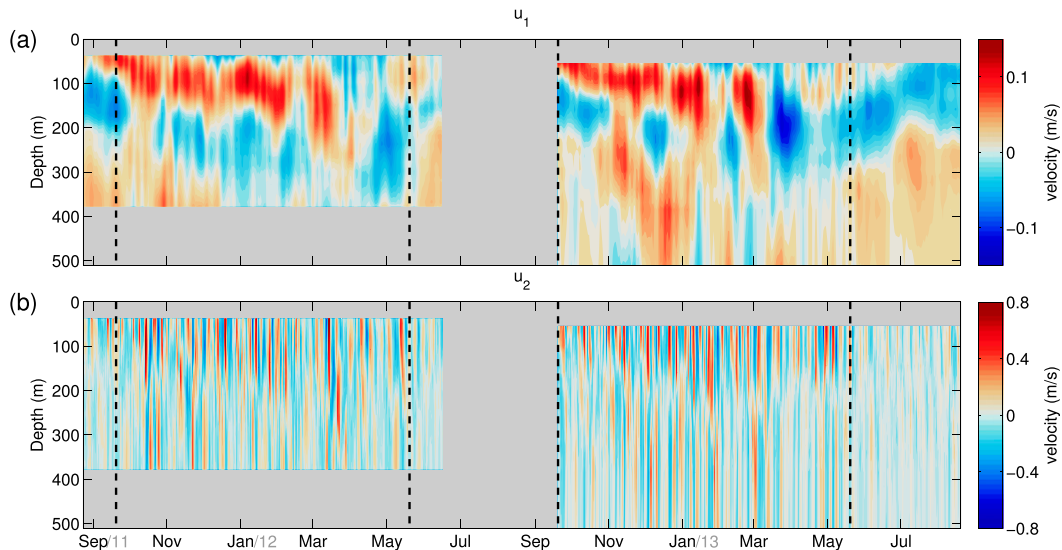
FIG. 6. Velocity decomposition for measured part of water column. (a) Mean exchange velocity u_1 and (b) fluctuating velocity u_2. Note different scales on color bars. Extrapolated parts of the water column are not included.

where u_{ex}, θ_{ex}, and S_{ex} are the extrapolated fields; $H = 800$ m; and the overbar represents a running mean over time scale τ (i.e., a boxcar filter). The mean exchange and fluctuating transports from Eqs. (11) and (12) were then calculated from these quantities. For example, the exchange and fluctuating salt transports are calculated as

$$F_1(t) = \int_H^0 u_1(z,t)S_1(z,t)W(z)\,dz, \quad \text{and} \quad (19)$$

$$F_2(t) = \int_H^0 \overline{u_2(z,t)S_2(z,t)}W(z)\,dz. \quad (20)$$

For this analysis, we use an averaging time scale τ of 25 days, based on peak energy in the shelf-driven circulation at 3–10-day periods (Jackson et al. 2014). Thus, as shown in Fig. 6, u_2 is predominantly a reversing, two-layer velocity field that is driven by shelf variability, while u_1 is the low-frequency exchange flow. (One can see, however, that the running average does not entirely eliminate energy at <25-day time scales in u_1—a more sophisticated low-pass filter could do this better but complicates the error analysis.) The choice of τ involves a trade-off between a longer averaging time scale to reduce the impact of shelf-forced flows and a shorter time scale to retain seasonal signals in glacial inputs and fjord conditions. Unlike the tides, the shelf-driven circulation is not a narrow-band signal, so separating it from other modes of circulation is difficult. Caution is required when assigning physical meaning to this time-scale decomposition.

The heat and salt storage terms were calculated by assuming that the variability observed at the moorings was representative of the variability upstream of the moorings, over the whole control volume. The salinity storage of Eq. (12) can be rewritten as $\overline{F}_{\text{Storage}} = (\partial\langle\overline{S}\rangle/\partial t)V_c$, where $\langle\overline{S}\rangle$ is the time- and volume-averaged salinity over the control volume V_c. Thus, by assuming that the volume-averaged salinity is approximately equal to the section-averaged salinity (i.e., $\langle\overline{S}\rangle \approx S_0$), we calculated the salt storage term as $\overline{F}_{\text{Storage}} = (\partial S_0/\partial t)V_c$. Following the same logic, the heat storage term is $\overline{H}_{\text{Storage}} = \rho c_p(\partial\theta_0/\partial t)V_c$. The upstream control volume V_c was estimated to be 330 ± 50 km^3 using the bathymetry in Fig. 2 and MODIS satellite imagery.

In calculating the storage terms this way, we make a significant assumption that water property variability at midfjord is, to first order, representative of the variability in the whole control volume. This assumption is supported by analysis from Jackson et al. (2014) and Sutherland et al. (2014b). The dominant temperature and salinity variability in the fjord arises from vertical displacements of the pycnocline. A comparison of mid- and upper-fjord moorings in Sermilik found a high coherence and lagged correlation in water properties between the two locations (Jackson et al. 2014). These pycnocline fluctuations occur over synoptic time scales but take less than a day to propagate upfjord (see below), and thus the pycnocline heaving is approximately uniform throughout the fjord on time scales longer than a day. Additionally, the shelf-forced flows not only drive heaving (i.e., thickness changes in the PW/AW layers), but they also advect variability in AW/PW water mass properties from the shelf through the main part of the fjord on synoptic time scales (Jackson et al. 2014).
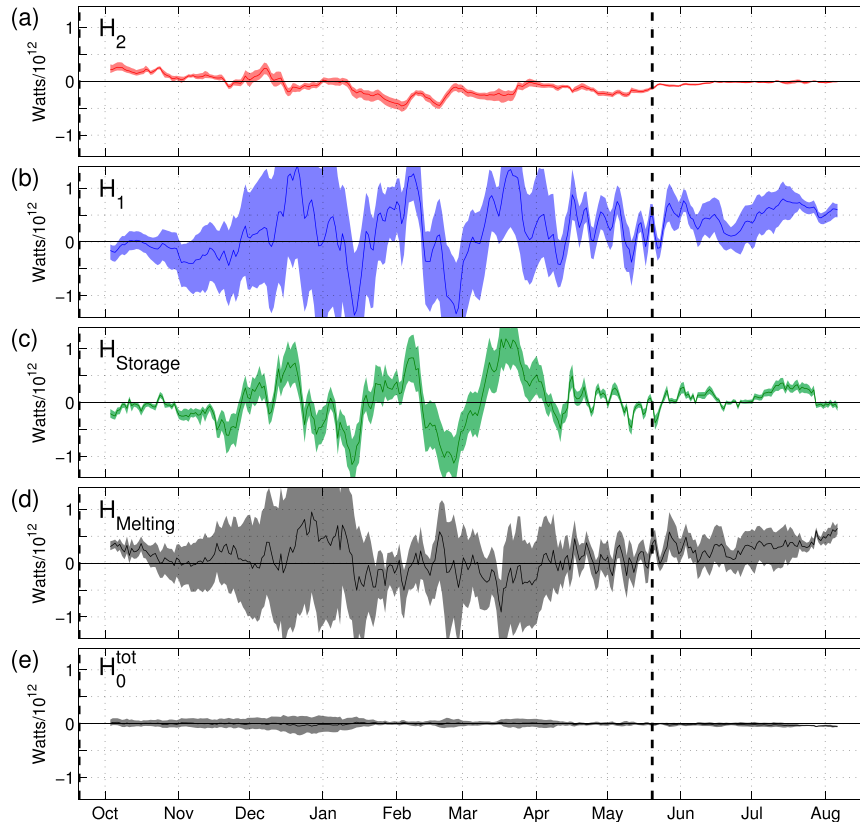
FIG. 7. Measured and inferred components of the heat budget [in the form of Eq. (15)] for 2012–13. (a)–(c) Directly measured fluctuating, exchange, and storage terms in heat budget. (d) Inferred heat for melting ice H_{melting}. (e) Inferred barotropic heat flux divergence H_0^{tot}. Error bars here and in subsequent figures are 95% confidence intervals. Colored time series are measured quantities; black are inferred.

The method used for calculating the storage terms here is based on observations from Sermilik and might not be justified in other systems or when measurements are made close to a glacier, in the region of convective plumes.

The measurable terms of the heat and salt budgets (F_1, H_1, F_2, H_2, F_{Storage}, H_{Storage}) for the second year are shown in color in Figs. 7 and 8. Using Eqs. (16)–(18), these quantities were used to infer freshwater fluxes of meltwater and runoff, as shown in Fig. 9. In calculating the freshwater fluxes, we assume that runoff enters the fjord at $-0.25° \pm 0.25°\text{C}$, the in situ freezing point of freshwater at 0–630 m depth (covering runoff that enters anywhere from the surface to the base of Helheim Glacier), and that meltwater enters at $-2.0° \pm 0.4°\text{C}$, based on the freezing point of seawater at a depth of 0–630 m and with a salinity of 30–35 (i.e., the property range of seawater that could drive melting). Additionally, the inferred freshwater fluxes were used to calculate the residual components of the heat and salt budgets: the heat to melt ice [$\overline{H}_{\text{Melting}}$, Eq. (4)] and the barotropic heat flux divergence [$\overline{H}_0^{\text{tot}}$, Eq. (14)] in Fig. 7 and the

barotropic salt flux (F_0) in Fig. 8. We neglect surface heat fluxes, though their potential impact is mentioned in section 4b and explored in appendix C.

Seasonal averages for the heat budget components, salt budget components, and freshwater fluxes are reported in Table 3.

b. Seasonal evolution of the heat/salt budgets

Before discussing the inferred freshwater fluxes, the dominant balances in the heat and salt budgets are examined. We focus on the second year of records (2012–13) that cover both nonsummer and summer months, but all of the main conclusions reported here about the nonsummer months were found in both years.

1) DOMINANT BALANCES IN THE NONSUMMER MONTHS

In the nonsummer months, the measured advective transports are balanced by changes in storage: within our ability to measure, $H_1 + H_2 \approx \overline{H}_{\text{Storage}}$ and $F_1 + F_2 \approx \overline{F}_{\text{Storage}}$. Consequently, the residual terms in the heat and
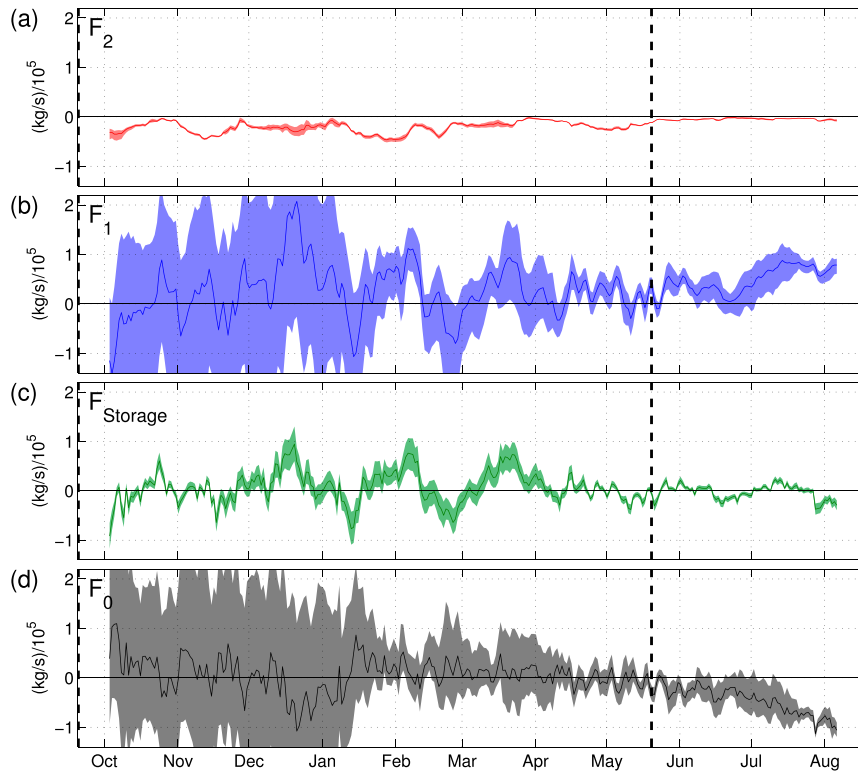
FIG. 8. Measured and inferred components of the salt budget [in the form of Eq. (12)] for 2012–13. (a)–(c) Directly measured fluctuating, exchange, and storage terms in salt budget. (d) Inferred barotropic salt transport F_0. As in Fig. 7, colored time series are measured quantities; black is inferred.

salt budgets (F_0, H_0^{tot}, and $\overline{H}_{\text{Melting}}$) are indistinguishable from zero within our error bars (Figs. 7, 8), as are the freshwater fluxes (Fig. 9). The budget results are summarized in the schematic of Fig. 10.

(i) Storage balances advective transports of heat and salt

Shelf forcing, which is strongest in the nonsummer months, has a strong imprint on the fjord budgets. The storage terms, which are leading-order components of the nonsummer budgets (Figs. 7, 8), are largely associated with the shelf-forced circulation. The shelf-forced pulses drive temperature and salinity variability through two (intertwined) mechanisms: large pycnocline fluctuations that change the relative thickness of the PW and AW layers, and rapid exchange with the shelf that advects shelf water into the fjord (Jackson et al. 2014). If the pycnocline heaves uniformly throughout the fjord, a simple expression for the volume-averaged temperature $\langle \theta \rangle$ is

$$\langle \theta \rangle = \frac{\theta_U h + \theta_L (H - h)}{H}, \qquad (21)$$

where h is the depth of the interface between layers, H is the total depth, and θ_U and θ_L are the average temperatures of the upper and lower layers, respectively. The assumption of uniform pycnocline heaving throughout the fjord was found by Jackson et al. (2014) to be a

TABLE 3. Averages from 2012–13 records over the nonsummer and summer for components of heat budget, components of salt budget, and freshwater fluxes. Confidence intervals include the standard error and the spread from the eight different extrapolation permutations.

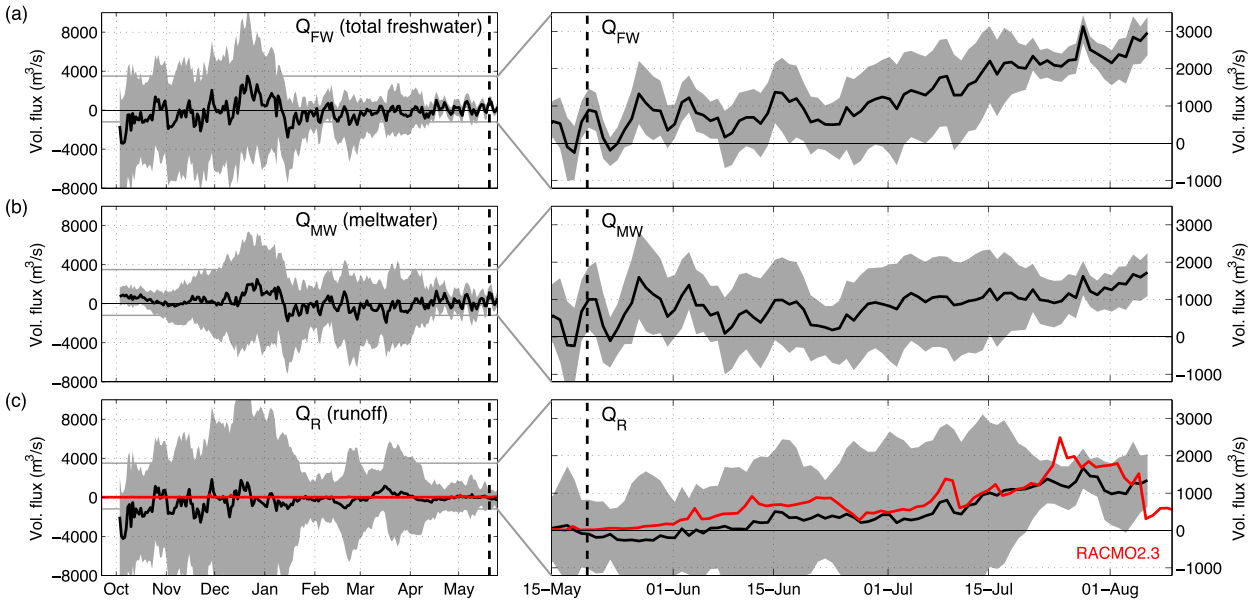|	Nonsummer	Summer
H_{Storage}	$-0.3 \pm 7.5 \times 10^{10}$ W	$9.9 \pm 3.6 \times 10^{10}$ W
H_2	$-9.1 \pm 2.0 \times 10^{10}$ W	$-3.1 \pm 0.9 \times 10^{10}$ W
H_1	$1.5 \pm 2.3 \times 10^{11}$ W	$4.8 \pm 1.5 \times 10^{11}$ W
H_0^{tot}	$0.0 \pm 2.3 \times 10^{10}$ W	$-2.2 \pm 1.6 \times 10^{10}$ W
H_{Melting}	$0.6 \pm 2.0 \times 10^{11}$ W	$3.1 \pm 1.4 \times 10^{11}$ W
F_{Storage}	$7.0 \pm 5.4 \times 10^3$ kg s^{-1}	$-2.9 \pm 3.2 \times 10^4$ kg s^{-1}
F_2	$-2.2 \pm 0.2 \times 10^4$ kg s^{-1}	$-4.9 \pm 0.6 \times 10^3$ kg s^{-1}
F_1	$2.4 \pm 3.5 \times 10^4$ kg s^{-1}	$4.7 \pm 1.5 \times 10^4$ kg s^{-1}
F_0	$0.6 \pm 3.3 \times 10^4$ kg s^{-1}	$-4.5 \pm 1.4 \times 10^4$ kg s^{-1}
Q_{FW}	-150 ± 1100 m^3 s^{-1}	1330 ± 450 m^3 s^{-1}
Q_{MW}	160 ± 900 m^3 s^{-1}	900 ± 540 m^3 s^{-1}
Q_R	-310 ± 2000 m^3 s^{-1}	430 ± 990 m^3 s^{-1}

FIG. 9. Inferred freshwater fluxes from 2012 to 2013: (a) total freshwater; (b) meltwater; and (c) runoff, along with runoff output from RACMO2.3 into Sermilik Fjord (upstream of cross section). Left panels show nonsummer period; right panels show summer months on a different scale. Thin horizontal gray lines in left panels indicate the y axis range from the right panels.

relatively good approximation in Sermilik: pycnocline displacements have been found to propagate up the fjord at the first baroclinic mode phase speed of $\sim 1\,\mathrm{m\,s}^{-1}$, so a signal would take 22 h to travel from the mouth to the head of the fjord [based on comparison of moored density records from the shelf, midfjord, and upper fjord in Jackson et al. (2014)]. This propagation

time scale is relatively short compared to the forcing time scale of 3–10 days. Thus, to first order, the interface heaves uniformly in the fjord on time scales longer than a day—something that has also been found in other fjords with shelf-driven circulations (e.g., Arneborg 2004).

Using the isopycnal of $\sigma_\theta = 27\,\mathrm{kg\,m}^{-3}$ as a proxy for the interface, we can reconstruct much of the average
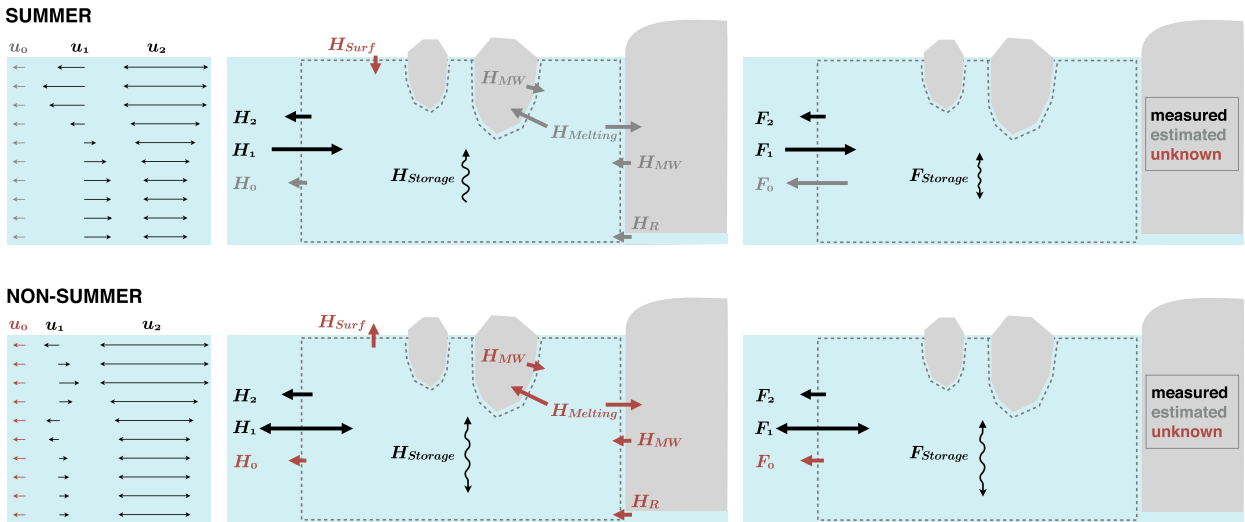

FIG. 10. Schematic of decomposed velocity field, heat budget, and salt budget for (top) summer and (bottom) nonsummer months. Terms are color-coded by whether they were directly measured (black), estimated from the residual of the budgets (gray), or unknown (red). For measured or estimated terms, the size of the arrow is approximately proportional to the magnitude. Note that the signs of H_0, H_R, and H_{MW} are dependent on the choice of a reference temperature; only their sum (H_0^{tot}) is independent of the reference temperature, and H_0^{tot} should always be negative. Summer is May–September; nonsummer is September–May.
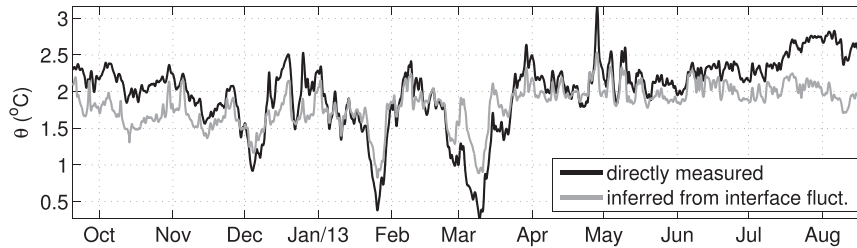
FIG. 11. Comparison of depth-averaged temperature $\langle\theta\rangle$ from measurements of temperature at moorings (black) and reconstructed from interface fluctuations following Eq. (21) (gray), assuming the upper-layer temperature is $-1°C$ and the lower layer is $3°C$.

temperature variability at the Sermilik moorings with Eq. (21) (Fig. 11). This reconstructed temperature record captures the vast majority of variability in the observed water column temperature, with a correlation coefficient of 0.82 ($p < 0.01$) and a statistically significant coherence for all periods between 18 h and 66 days. We do not, however, expect these measured and inferred records to match exactly, in part because of temperature changes within each layer.

Although a significant portion of this variability is transient, averaging over 25 days does not eliminate the heat/salt content variability. The nature of this storage term is illustrated by comparing a shorter averaging time scale τ of 2 days with the standard τ of 25 days (Fig. 12). When the averaging time scale is short, $\overline{H}_{Storage}$ fluctuates with the shelf-driven circulation on synoptic time scales. It has an average absolute value of 1.9×10^{12} W and frequently exceeds 5×10^{12} W. For comparison, the heat required to melt $1000 \, m^3 \, s^{-1}$ of ice (the order of the total ice discharge into Sermilik) is 3.6×10^{11} W, which is an order of magnitude smaller than the storage term. When a longer averaging time scale of 25 days is applied, the impact of shelf-driven circulations is diminished, reducing the amplitude of both $\overline{H}_{Storage}$ and $H_1 + H_2$. Nevertheless, the advective heat transports are still balanced by changes in storage within our error bars. Even averaging over the entire season (Table 3) does not allow a residual to be distinguishable from zero.

(ii) Structure of the advective transports

In the nonsummer months, the mean exchange transports associated with u_1 do not have a consistent sign. The H_1 and F_1 fluctuate between positive and negative (Figs. 7, 8), with large error bars due to shelf-forced variability and a significant spread from the extrapolation techniques. During this period, the mean exchange velocity u_1 is almost an order of magnitude smaller than the fluctuating component (Fig. 6). The same structure, however, emerges when both non-summer periods are averaged: in Fig. 13d, the average u_1 profiles show upfjord flow centered at 100 m, with weaker outflowing velocity at ~220 m and inflowing velocity below ~300 m. There also appears to be outflow near the surface, though this part of the water column is poorly sampled, which might suggest multiple outflows from the glacier. However, the u_1 field in the winter is not necessarily a signal of a buoyancy-driven flow from freshwater inputs—given the small magnitude of u_1 relative to synoptic-scale flows, u_1 could be a residual from other fjord dynamics or partially a sampling bias (see section 5a).

Although the exchange transports do not have a consistent sign and are not necessarily driven by glacier buoyancy forcing, there are consistent patterns in the water properties that are imported and exported by the
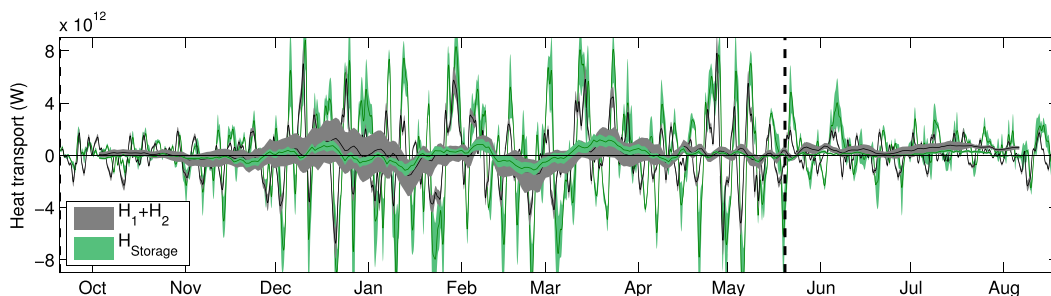

FIG. 12. Comparison of heat storage ($H_{Storage}$) and cross-section transport ($H_1 + H_2$) for averaging time scales of both 2 days and 25 days. The shorter averaging time scale has larger amplitude fluctuation while the longer time scale is reduced in amplitude (and plotted on top).
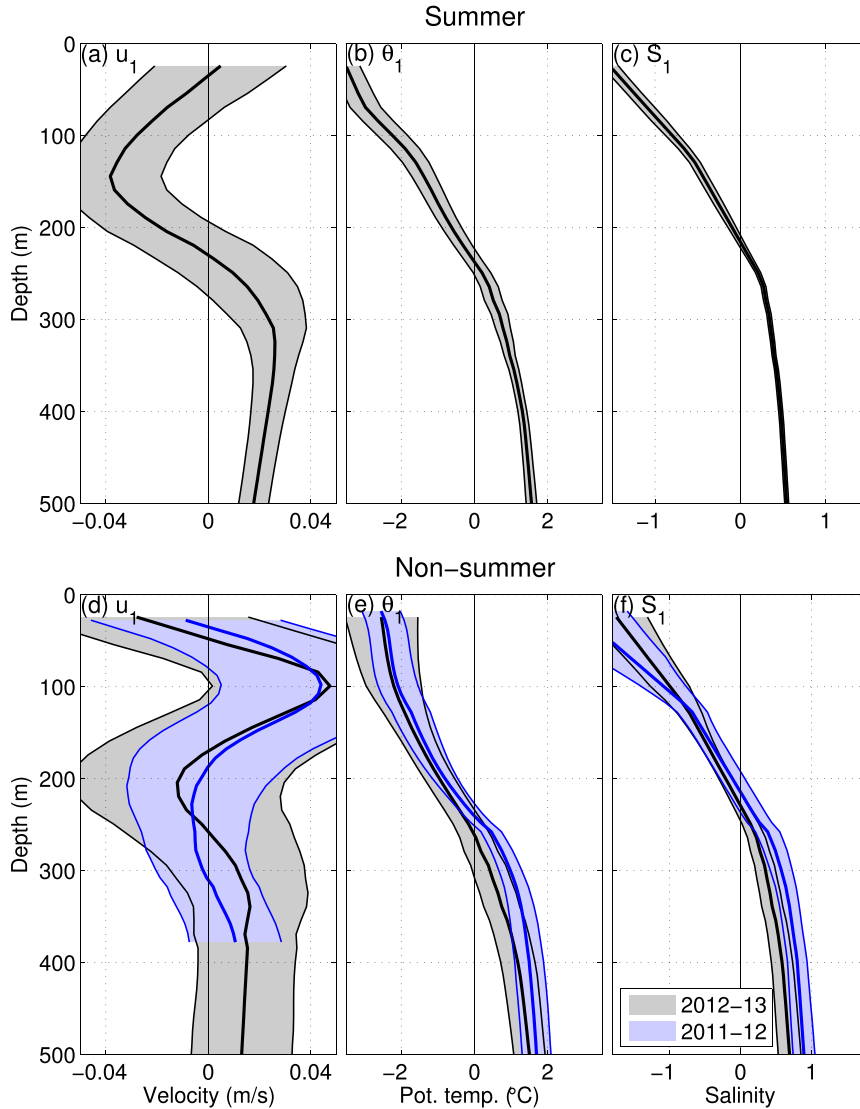
FIG. 13. Average of u_1, θ_1, and S_1 fields during (a)–(c) the summer months (20 May to 20 Aug) and (d)–(f) the nonsummer months (20 Sep to 20 May). Error bars show one standard deviation of the exchange fields over the time period (*not* the standard deviation of the full fields which include u_2, θ_2, and S_2).

u_1 field, as shown in Fig. 14. In the fall months, deep AW and the warm surface layer on the shelf are imported into the fjord while a layer of glacially modified water that diverges from shelf properties is often exported between 100 and 200 m. The early winter is difficult to interpret, but a clear pattern emerges again in the February–May panel of Fig. 14. During this late winter and spring period, the fjord water properties resemble the shelf water masses with modification from submarine meltwater. The properties that match the shelf are preferentially inflowing while the modified properties (to the left in θ–S space) are, on average, outflowing.

For the fluctuating transports, we observe correlations among u_2, θ_2, and S_2 that result in transports of heat and salt away from the glacier (Figs. 7, 8). The structure of this signal is shown in Fig. 15, where $\overline{u_2\theta_2}$ and $\overline{u_2 S_2}$ are plotted as a function of depth and time. One can see export of heat and salt in the upper layer, with peak values between 100 and 250 m. In the nonsummer months, the total fluctuating heat transport (H_2 in Fig. 7 or the vertical integral of Fig. 15) typically exports 1–3×10^{11} W, equivalent to the latent heat to melt/freeze 270–820 $m^3\,s^{-1}$ of ice.
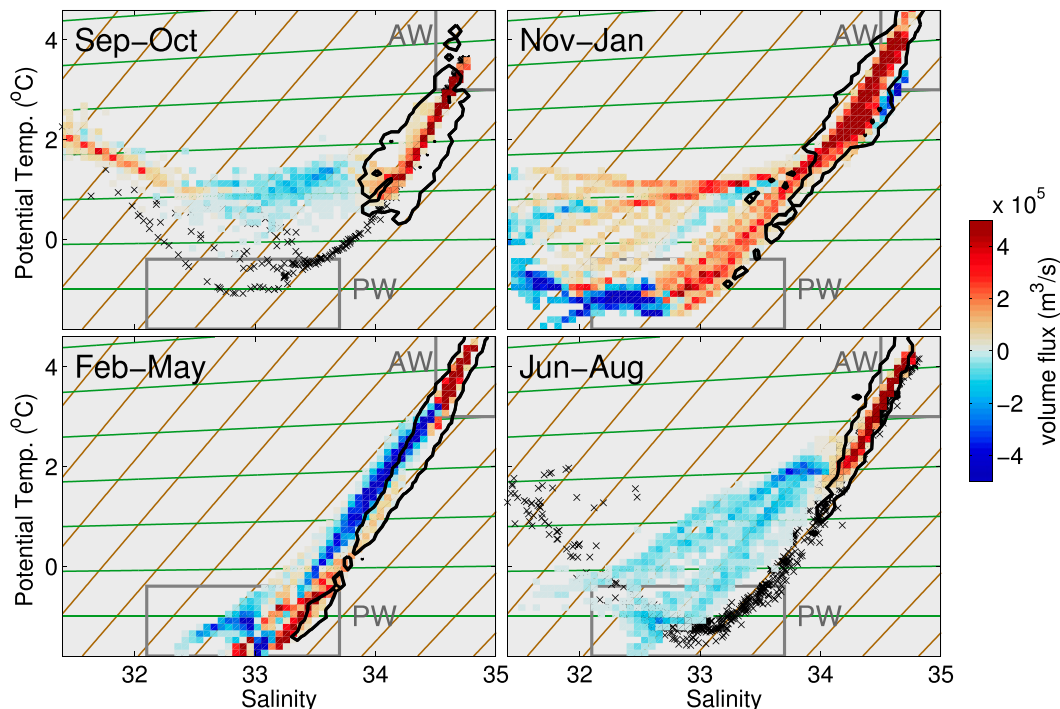
FIG. 14. Volume transport from the u_1 field binned in θ–S space for four different periods in 2012–13. The midfjord θ–S properties are binned in the same manner as Fig. 5, but the color is the average volume flux from the u_1 field in that bin, defined as $\sum(u_1\,dA_x)$ for all points within the θ–S bin. Positive values are toward the glacier, into the control volume. As described in Fig. 5, the black contour encloses bins with >0.1% of shelf measurements and the black crosses in the first and last panel are from CTD surveys of the shelf in September 2012 and August 2013, respectively. Brown lines are meltwater mixing lines and green lines are runoff mixing lines. Gray boxes show typical AW and PW properties.

Part of this observed signal could arise from neglecting cross-fjord variability while sampling on the eastern side of the fjord—the net fluctuating transport might be closer to zero if we had full coverage of the cross section. If pycnocline heaving is accompanied by cross-fjord geostrophic tilt, then assuming that our eastern-side measurements are representative of the whole cross section could lead to spurious results for F_2 and H_2. This possibility is explored in section 5a and appendix B.
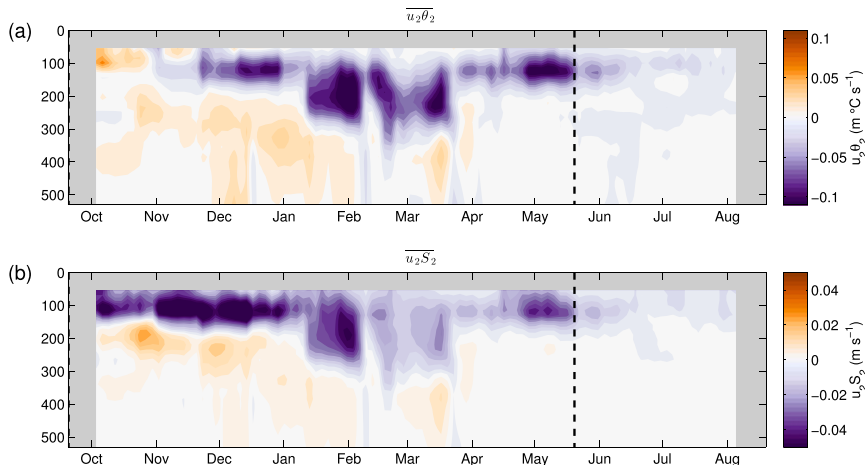

FIG. 15. Correlations in the fluctuating velocities and water properties: (a) $\overline{u_2\theta_2}$ and (b) $\overline{u_2 S_2}$ as a function of depth and time for the second year of records. Positive values are heat/salt fluxes toward the glacier or into the control volume.
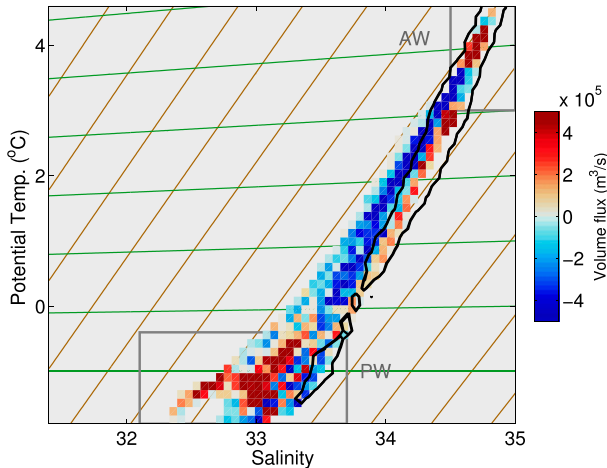
FIG. 16. Volume transport from the u_2 field over bins in θ–S space for February–May 2013. The midfjord θ–S properties are binned in the same manner as Fig. 5, but color is the average volume flux from the u_2 field, defined as $\sum(u_2\,dA_x)$ for all points within a θ–S bin. While u_2 has a zero time average at any depth, the time average in θ–S bins is not zero. Positive values are toward the glacier, into the control volume. As described in Fig. 5, the black contour encloses bins with >0.1% of shelf measurements. Brown lines are meltwater mixing lines and green lines are runoff mixing lines. Gray boxes show typical AW and PW properties.

We find that the fluctuating velocity plays a role in exporting glacially modified water, which could also explain some of the heat/salt export in F_2 and H_2. Figure 16 shows a θ–S diagram for January–May with u_2 transport mapped onto the θ–S bins. Below the surface layer (i.e., $S > 33.5$), the u_2 field is positive on average when fjord θ–S properties match the shelf. When fjord properties diverge from the shelf and look glacially modified, u_2 is typically negative. Thus, there are persistent correlations between u_2 and the presence of glacially modified water, suggesting that the fluctuating velocity exports meltwater during this nonsummer period.

We expect the fluctuating export of glacially modified water to result in a flux of heat and salt away from the glacier. This might seem counterintuitive, since the glacier is ultimately a net source of freshwater and sink of heat. However, based on the slope of the ambient shelf properties in θ–S space, we expect modification from meltwater or runoff to cause warm, salty anomalies in the fjord relative to the shelf (in most of the water column; e.g., Jenkins 1999). This can be seen in the θ–S diagrams: when deep AW is mixed along the meltwater or runoff mixing lines, the water becomes fresher and cooler, but the mixture, now a lower density than the original AW, will be a warm, salty anomaly compared to ambient shelf water of this new density. Thus, we expect

that, if u_2 fluxes heat and salt down the gradients between the ambient shelf water and glacially modified fjord water, it would result in a net export of heat and salt.

While we have evidence that the u_2 field exports glacially modified water, we do not attribute the entire signal for H_2 and F_2 to this process. Sampling biases, as discussed above, or other processes, such as mixing in the control volume or temporal variability in shelf properties, are likely contributors to the observed fluctuating transports.

(iii) Estimating the residual terms in the heat/salt budgets

While it is impossible to infer a residual from the measurable terms in the heat or salt budgets, we can put some constraints on the unknown terms of the non-summer budgets. The latent heat for melting ice $\overline{H}_{\mathrm{Melting}}$ is constrained to be less than 1×10^{12} W for most of the winter (Fig. 7) and, physically, it must be positive; it could be a trivial term or it could be of a similar magnitude as the advective and storage terms. Throughout the year, we expect there to be melting of ice that extracts heat from the ocean, but we cannot measure it within the "noise" of other fjord processes during the nonsummer months. The barotropic heat flux divergence, also indistinguishable from zero because the freshwater fluxes are indistinguishable from zero [see Eq. (14)], is constrained to be less than 1×10^{11} W—that is, an order of magnitude smaller than other terms in the heat budget (Fig. 7).

During the winter, there are likely $O(10^{10}$–$10^{11})$ W leaving the control volume from surface fluxes (appendix C), which would be equivalent to the latent heat for $O(10$–$100)$ m^3 s^{-1} of meltwater. Although these surface fluxes are not a leading-order component of the heat budget, they would need to be included to measure the meltwater with an accuracy of $O(100)$ m^3 s^{-1}. Additionally, in winter, the volume of sea ice formed in the fjord might not be negligible compared to the meltwater volume flux. In our formulation of the budgets, sea ice formation would appear as a negative contribution to the total inferred freshwater flux.

2) DOMINANT BALANCES IN THE SUMMER MONTHS

In the summer salt budget, we measure F_1, F_2, and $\overline{F}_{\mathrm{Storage}}$, and we are able to estimate F_0 as a residual (Fig. 8). Since F_0 is proportional to $\overline{Q}_{\mathrm{FW}}$, this means that the total freshwater flux becomes distinguishable from zero in the summer months. The salt budget is primarily a balance between imported salt from the exchange F_1 and

exported salt from the barotropic flux F_0 (Fig. 8 and schematic in Fig. 10). The storage term fluctuates between positive and negative, while the fluctuating transport exports a relatively small quantity of salt.

The leading-order terms in the summer heat budget are the exchange transport H_1 the storage term $\overline{H}_{Storage}$, and the heat for melting $\overline{H}_{Melting}$ (Fig. 7 and schematic in Fig. 10). The exchange transport imports heat into the control volume, part of which goes into warming the control volume (hence the positive $\overline{H}_{Storage}$) and part to melting ice. The fluctuating transport H_2 and the barotropic heat flux divergence H_0^{tot} both play a minor role in exporting heat from the control volume.

(i) Storage

The shelf-forced flows, primarily captured in the u_2 field, become weaker in the summer (Fig. 6). The corresponding reduction in water property variability leads to smaller storage terms, as shown in Fig. 12 comparing 2- and 25-day averaging time scales. With the short averaging time scale, the measured cross-section transports equals $\overline{H}_{Storage}$ (with a 1-day lag) within the error bars, as in the winter; estimating the residual $\overline{H}_{Melting}$ is impossible at this short averaging time scale. On the other hand, with a longer averaging time scale of 25 days, the impact of shelf-forcing is diminished, and there is a statistically significant difference between heat storage and cross-section transport, which allows us to infer the residual heat for melting in summer. Nevertheless, $\overline{H}_{Storage}$ (and also $\overline{F}_{Storage}$) remain leading-order terms throughout the year. A summer-long average further reduces the storage terms (Table 3) but hinders our ability to see any seasonal evolution.

(ii) Advective transports

In the summer, when shelf-forcing is reduced, u_1 and u_2 are of a similar magnitude, and there is a more clear and evolving structure in the mean exchange (Fig. 6). In June, there is a thick outflowing layer from approximately 250 to 100 m depth, with inflow above and below. Over the course of the summer, this outflowing layer thickens and shoals, extending from approximately 200 m to above the range of our ADCP measurements. We cannot exclude the possibility that there is another inflow or inflow/outflow in the upper tens of meters, and our calculation of the heat and salt transports attempts to take into account this uncertainty by including a variety of extrapolation techniques (section 4a). The average profile of u_1 over the entire summer (Fig. 13) shows a thick outflowing layer above a deep inflowing layer. The outflow is subsurface intensified, resembling the glacier-driven flow in the modeling study of Carroll et al. (2015).

In the summer, the observed exchange flow imports heat and salt into the control volume, as shown by the positive values for H_1 and F_1 in Figs. 7 and 8. This is the result of warm, salty water inflowing at depth and relatively cooler, fresher water outflowing in the upper layer. The average summer profiles of u_1, θ_1, and S_1 that form the exchange transports are shown in Fig. 13. Variables θ_1 and S_1, which are the time-averaged fields with the depth-average removed, are positive when u_1 is upfjord and negative when u_1 is outflow, resulting in an overall import of heat and salt from the exchange flow.

This exchange flow in the summer consists of inflowing AW and outflowing glacially modified water. We illustrate this by mapping the mean transport from the u_1 field onto θ–S diagrams in Fig. 14. One can see that, in the panel for June–August, the inflowing water at depth has AW properties that match the shelf. The outflowing water falls in the part of θ–S space that diverges from the shelf properties in a manner consistent with modification from meltwater and runoff (Straneo et al. 2011): it is likely a mixture of the deep inflowing AW and glacial freshwater inputs.

The fluctuating transports export small quantities of heat and salt, consistent with the export of glacially modified water, as discussed in section 4b1. These fluctuating transports are an order of magnitude smaller than the exchange and storage for most of the summer.

(iii) Estimating the residual terms in the heat/salt budgets

In the summer salt budget, the barotropic salt transport can be inferred from the residual of the exchange, fluctuating, and storage terms. Export of salt from the barotropic transport primarily balances the import of salt from the exchange flow and changes in salt storage.

The measured terms in the salt and heat budgets allow for estimates of $\overline{H}_{Melting}$ and H_0^{tot}. The latent heat for melting becomes distinguishable from zero in July and is a leading-order term in the heat budget by August. The heat flux divergence is negative, by definition [Eq. (14)], and an order of magnitude smaller than the exchange, storage, and latent heat for melting terms.

Surface heat fluxes have not been included in these calculations, but they are expected to be an order of magnitude smaller than the estimated latent heat for melting (appendix C). Since the control volume would gain heat at the surface during the summer, the neglect of the surface heat flux should lead to a small underestimation of the meltwater flux.

c. Magnitude and variability of freshwater fluxes

In the nonsummer months, $\overline{Q}_{FW}$, $\overline{Q}_{MW}$, and $\overline{Q}_R$ are indistinguishable from zero (Fig. 9), with the 10-month-average freshwater flux only constrained to be less than $\sim 1000\, m^3\, s^{-1}$ (Table 3). While the error bars are still significant during the summer, the fluxes become more narrowly constrained and distinguishable from zero. The total freshwater entering the fjord increases from $800 \pm 500\, m^3\, s^{-1}$ in June to $2400 \pm 500\, m^3\, s^{-1}$ in late July and early August (Fig. 9). The lower bound on the total freshwater estimate in this latter period exceeds the upper bound from January through May.

Runoff does not become distinguishable from zero until late July, reaching a value of $\overline{Q}_R = 1200 \pm 700\, m^3\, s^{-1}$ in August. The concurrent RACMO2.3 output for runoff entering upper Sermilik Fjord (i.e., into our control volume) is shown in Fig. 9c and agrees with our estimate of runoff within the uncertainty.

The submarine meltwater flux first becomes distinguishable from zero in late July. In June and early July, $600 \pm 600\, m^3\, s^{-1}$ of meltwater enters the fjord. In late July and August, Q_{MW} becomes more narrowly constrained, reaching $1500 \pm 500\, m^3\, s^{-1}$. It is important to note that this meltwater flux is the sum of both glacier and iceberg melt—we make no claims that this is an estimate of Helheim Glacier's melt rate since we cannot separate the sources of submarine melting.

While there is a significant increase in the total freshwater flux over the summer, the meltwater and runoff fluxes do not have a discernible seasonality within their error bars. The seasonality in the total freshwater could be entirely related to runoff—from runoff itself and/or from runoff increasing glacier submarine melting (e.g., Xu et al. 2012; Sciascia et al. 2013). It is also possible that submarine melting increases during the summer for other reasons; for example, iceberg melting might increase as the upper 200 m warms as a result of glacial modification (see Figs. 2b,c).

5. Discussion

a. Errors and uncertainties

1) RESOLVING THE FJORD CROSS SECTION

The error bars in our estimates are an integral part of the analysis. Uncertainties and errors have been underemphasized and likely underestimated in many previous studies that infer submarine melt rates from measurements of ocean heat transport. In our calculations, the largest source of uncertainty is from incomplete coverage of the water column and the required extrapolation. Most previous studies have used synoptic surveys, which sometimes provide better spatial resolution of a fjord cross section but no temporal resolution. Here, we have somewhat limited spatial coverage but a more comprehensive picture of the system's time variability.

For the cross-section transports, our spatial coverage is lacking in two ways. First, we do not sample the surface layer: in velocity, we are missing the range of 0–27 m and 0–39 m in the first and second years, respectively; in salinity and temperature, we are missing 0–13 m and 0–50 m in the first and second years. We try to account for this by extrapolating with several different techniques and including their spread in our error bars. A comparison with the shipboard surveys suggests that this extrapolation spread should do well at capturing the surface properties during the nonsummer and should do well below 10 m in the summer, but it likely overestimates salinity in the top 10 m during the summer. Second, we neglect lateral variability between our moorings and assume that these records are representative of the entire cross section, thereby neglecting cross-fjord variability. In calculating the storage term, we make an additional assumption by estimating the control volume's water properties from the records at the southern boundary, that is, at the mooring location.

To evaluate the limitation of our cross-fjord coverage, we estimate the magnitude of cross-fjord gradients and their potential manifestation in our observations and calculations. Assuming that the along-fjord velocity is in geostrophic balance, we estimate the cross-fjord tilt in the pycnocline to be ~ 30 m across the fjord width during peak velocity shears in winter (appendix B). A simple model for the shelf-forced flows in appendix B indicates that the observed exchange velocity and fluctuating transports in the nonsummer months could be an artifact of our sampling locations, which are biased toward the eastern side of the fjord. In this two-layer model, there is no net mass, heat, or salt transport in either layer; however, if the pycnocline heaving has a cross-fjord tilt, one would observe mean velocities and fluctuating transports in the depth range of pycnocline excursions when measuring off-center in the fjord. The sign, magnitude, and structure of these signals in the model are similar to our nonsummer observations of a mean inflow between 50 and 200 m and fluctuating export of heat/salt at middepth. The mean exchange velocities observed in summer, however, could not be attributed to this sampling bias.

To reduce the error bars and better constrain the freshwater fluxes in a system like Sermilik, one would need to have both good spatial and good temporal coverage—either one alone is not sufficient. Mooring arrays that cover the upper tens of meters at the surface,

as well as the cross-fjord structure, would be ideal (but logistically difficult). However, this cannot come at the expense of coverage in time. The temporal variability in a system like Sermilik Fjord imprints on the budgets in many ways, for example, in the important role of heat/salt storage or fluctuating transports, so any snapshot of cross-section transports should not be used to infer freshwater fluxes.

2) CONTROL VOLUME SIZE

In this analysis and all previous studies, any variability in the size of the control volume has been neglected; the volume of liquid water (V_c) on the landward side of the cross section is assumed to remain constant. There could, however, be significant variability in V_c from changes in the glacier terminus position, from changes in iceberg volume, or from changes in sea surface height. If V_c is allowed to vary in time, the full mass budget from Eq. (1) becomes

$$\int_{A_x} u \, dA + Q_{FW} = \frac{\partial V_c}{\partial t} \qquad (22)$$

and the changes in V_c can be written as the sum of three components:

$$\frac{\partial V_c}{\partial t} = -\frac{\partial V_{glac}}{\partial t} - \frac{\partial V_{iceb}}{\partial t} + \frac{\partial \eta}{\partial t} A_{Surf}, \qquad (23)$$

where $\partial V_{glac}/\partial t$ is the change in glacier volume below sea level from terminus advance and retreat, $\partial V_{iceb}/\partial t$ is the change in iceberg volume below sea level within the control volume, η is the sea surface height, and A_{Surf} is the surface area of the control volume. Changes in the volume of ice result in V_c changes of the opposite sign, because we have defined V_c as the volume of *liquid* water upstream of a fixed cross section.

While we cannot directly evaluate these terms for Sermilik Fjord, we can estimate their magnitude. Jackson et al. (2014) find an increase in sea surface height of ~15 cm for synoptic downwelling events with time scales of 3–10 days, corresponding to $(\partial \eta/\partial t)A_{Surf} \approx 200 \, \mathrm{m^3 \, s^{-1}}$. With our averaging time scale of 25 days, this would reduce to ~40 m³ s⁻¹ and thus be insignificant in the time-averaged mass budget. The volume variability resulting from glacier advance/retreat can be estimated with measurements of the glacier terminus position. Helheim Glacier has a typical summer retreat of 2.2 km over an average of 120 days (Schild and Hamilton 2013), which would correspond to $\partial V_{glac}/\partial t = -760 \, \mathrm{m^3 \, s^{-1}}$, assuming a submarine glacier terminus area of 3.6 km². During our observational period in the summer of 2013, Helheim Glacier retreated by more than 1 km over less than 3 weeks (Bevan et al. 2015), corresponding to

$\partial V_{glac}/\partial t < -2000 \, \mathrm{m^3 \, s^{-1}}$. If the freshwater fluxes are $O(1000) \, \mathrm{m^3 \, s^{-1}}$, then $\partial V_{glac}/\partial t$ could be a leading-order term in the mass budget at certain times. The volume change in icebergs $\partial V_{iceb}/\partial t$ is the hardest term to estimate and might partially counteract changes in glacier volume: when the glacier retreats, the calving rate typically increases and the volume of icebergs in the control volume might increase. It is difficult, however, to evaluate the extent to which these components balance, and we expect that at times their sum $\partial V_c/\partial t$ will be of the same magnitude as Q_{FW}.

Although variability in control volume size ($\partial V_c/\partial t$) might be a leading-order term in the mass budget, its effect is drastically diminished when inferring freshwater fluxes with the methods in this paper. When variability in V_c is included, the equation for inferring Q_{FW} from the combined salt and mass budgets [Eq. (16)] becomes

$$\overline{Q}_{FW} = \frac{1}{S_0}(F_1 + F_2 - \overline{F}_{Storage}) + \left(1 - \frac{\langle S \rangle}{S_0}\right)\frac{\partial V_c}{\partial t}, \qquad (24)$$

where $\langle S \rangle$ is the average salinity in V_c (see derivation in appendix A). The last term on the right side is the only difference between this equation, which accounts for volume changes, and Eq. (16), which neglects volume changes. One can see that the impact of $\partial V_c/\partial t$ on the freshwater flux calculation will go to zero as the average cross-section salinity (S_0) approaches the volume averaged salinity ($\langle S \rangle$). Physically, this condition means that the along-fjord horizontal salinity differences must be small compared to the depth-averaged salinity. Based on surveys of Sermilik Fjord (e.g., Fig. 2; Straneo et al. 2011; Sutherland et al. 2014b), the horizontal salinity gradient is small and $[1 - (\langle S \rangle/S_0)] < 0.02$. Therefore, even though $\partial V_c/\partial t$ might be an order of magnitude larger than Q_{FW} in the mass budget, the error on the freshwater flux calculation from neglecting $\partial V_c/\partial t$ will be at least an order of magnitude smaller than the total freshwater flux. This allows us to neglect variability in the control volume size when estimating the freshwater fluxes from heat and salt budgets.

The factor of $[1 - (\langle S \rangle/S_0)]$ might be significantly larger in other systems. If there is a strong horizontal salinity gradient, the cross-section salinity at the edge of the control volume could be substantially higher than the volume-averaged salinity such that changes in the control volume size might not be negligible. The underlying principle is that we do not attempt to measure the barotropic velocity (u_0), while we do rely on measuring the depth-average water properties θ_0 and S_0. If these measured water properties θ_0 and S_0 are sensitive to small displacements in the location of the cross

section, then the overall results will be sensitive to changes in the control volume size.

b. Interpreting the observed freshwater fluxes

Previous estimates of submarine melting in fjords purport to measure glacier (as opposed to iceberg) melting and often present their results as a melt rate (e.g., $m\,yr^{-1}$) across the glacier's terminus. Our results, however, are reported in terms of a total liquid meltwater flux from glaciers and icebergs, with no attempt made to distinguish between the two. This, plus the fact that we do not expect the same meltwater fluxes in different fjord/glacier systems, complicates any comparison between our meltwater fluxes and previous results. Studies from other Greenlandic and Alaskan fjords (Motyka et al. 2003; Rignot et al. 2010; Motyka et al. 2013; Xu et al. 2013; Bartholomaus et al. 2013; Inall et al. 2014) report meltwater fluxes between 5 and $830\,m^3\,s^{-1}$, with our measured meltwater flux falling at the upper end of this range. In a more apt comparison, our observed meltwater flux is notably higher than a previous estimate for Sermilik Fjord: Sutherland and Straneo (2012) find a meltwater flux of $86\,m^3\,s^{-1}$ in August of 2009, which is below the range of our summer estimates in July and August.

Perhaps a more interesting comparison is between our measured meltwater flux and estimates of total ice discharge (iceberg calving plus submarine melting) from the glaciers that drain into Sermilik. Mernild et al. (2010) estimate an annual average ice discharge of $821 \pm 82\,m^3\,s^{-1}$ (water equivalent) from Helheim and $253 \pm 48\,m^3\,s^{-1}$ from the two smaller glaciers in Sermilik. Other measurements of Helheim ice discharge (e.g., Enderlin et al. 2014; Enderlin and Howat 2013) agree with those discharge numbers, and the seasonal cycle of discharge is less than ~20% (Bevan et al. 2015; Moon et al. 2014). Our summer-average estimate of $Q_{MW} = 900 \pm 540\,m^3\,s^{-1}$ is similar in magnitude to the total estimated ice discharge from the glaciers; based on $1100\,m^3\,s^{-1}$ of ice discharge and lower/upper bounds of our estimate, between 30% and 100% of the total ice discharge melts within the fjord. In a steady state, the difference between the total ice discharge and the submarine melting within the control volume is the solid iceberg flux that leaves the control volume. Our results suggest that a substantial portion (>30%) of the total ice flux from the glaciers either melts at the terminus or melts from icebergs within the fjord. The upper limit of 100% of the ice discharge melting within the fjord is unrealistic because at least some icebergs do leave the fjord (Sutherland et al. 2014a).

The measured meltwater flux undoubtedly contains iceberg meltwater, though the fraction cannot be quantified with our method. A recent attempt to measure submarine melting of icebergs in Sermilik suggests that iceberg melting might be a significant fraction of our total meltwater flux. Enderlin and Hamilton (2014) find that 10 large icebergs, which constitute 5% of the mélange surface area, contribute $25\,m^3\,s^{-1}$ of meltwater. This result indicates that icebergs throughout the fjord might contribute $O(100)\,m^3\,s^{-1}$ or more of meltwater, illustrating the potentially important but unconstrained role of icebergs in the meltwater flux. If icebergs do contribute a significant meltwater flux, then the total inferred meltwater flux Q_{MW} would vary as a function of L, the distance of ocean measurements from the glacier.

Last, as shown in Fig. 9, our runoff estimate agrees with runoff output from RACMO2.3, within our error bars. As another point of comparison, Mernild et al. (2010) uses SnowModel to estimate an annual average runoff entering upper Sermilik Fjord from 1998 to 2008 of $3.2 \times 10^9\,m^3\,yr^{-1}$, equivalent to ~$410\,m^3\,s^{-1}$ if evenly distributed over three summer months. While our average runoff estimate over the whole summer is not distinguishable from zero, in early August it is constrained to $\overline{Q}_R = 1200 \pm 700\,m^3\,s^{-1}$, which is larger than the SnowModel estimate (though the time periods being compared do not overlap).

In August, the runoff and submarine meltwater fluxes are of the same magnitude: their ratio is $Q_R/Q_{MW} = 1.1 \pm 0.8$. This ratio of Q_R/Q_{MW} is smaller than the ratio found in previous observational studies of glacial fjords, which fall between 2 and 31 (Motyka et al. 2013; Xu et al. 2013; Rignot et al. 2010; Motyka et al. 2003). Our measured ratio suggests that runoff is not necessarily the predominant source of buoyancy forcing to the fjord during the summer. If iceberg meltwater is greater than glacier meltwater, however, there could be a region near the glacier where the ratio is larger and runoff is more dominant.

c. Across Greenland's fjords: Previous methods and future studies

Here we attempt to generalize some of our results and explore how the dominant balances in the heat and salt budgets might change in other systems. This has important practical implications for assessing when various terms in the budgets can be dropped—both in future studies and past attempts.

All previous studies have used simplified budgets to infer meltwater fluxes. One approach is to directly equate some portion of the cross-section heat transport to the heat extracted for melting (e.g., Sutherland and Straneo 2012). Other approaches employ both heat and salt budgets and retain more components of the budgets (e.g., Motyka et al. 2003; Rignot et al. 2010; Xu et al.
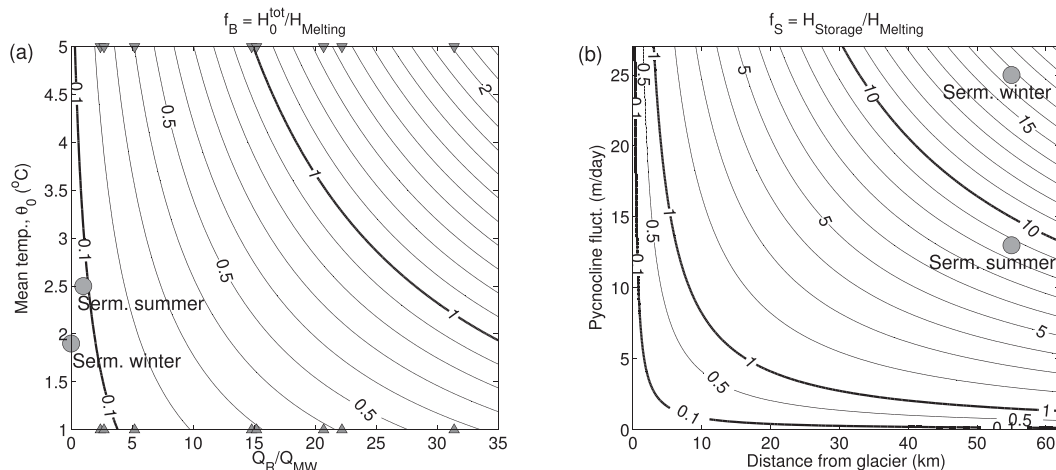
FIG. 17. (a) Ratio of barotropic heat flux divergence to heat for melting $f_B = H_0^{tot}/H_{Melting}$ as a function of mean cross-section temperature θ_0 and Q_R/Q_{MW}. This is based on Eq. (25) with values of $\theta_R = -0.5°C$ and $\theta_{MW} = -1.5°C$. Gray circles indicate Sermilik summer and winter in this parameter space. Gray triangles along the x axis indicate published values of Q_R/Q_{MW} from Motyka et al. (2003), Rignot et al. (2010), Motyka et al. (2013), Bartholomaus et al. (2013), and Xu et al. (2013). (b) Ratio of heat storage to heat for melting $f_S = H_{Storage}/H_{Melting}$ as a function of the amplitude of interface fluctuations and the distance of the cross-section measurements from the glacier. This is based on Eq. (27) with values of $W = 7.5$ km, $Q_{MW} = 400$ m³ s⁻¹, and $\Delta\theta = 5°C$. The black dots show our observations in Sermilik winter and summer in this parameter space.

2013; Motyka et al. 2013). In all cases, the storage terms ($F_{Storage}/H_{Storage}$), surface heat fluxes (H_{Surf}), and fluctuating transports (F_2/H_2) have been neglected. Additionally, the advective fluxes are never included completely, with potential problems arising from the neglect of, or ambiguity in handling, the barotropic heat fluxes.

1) BAROTROPIC HEAT FLUX DIVERGENCE

The barotropic heat flux divergence H_0^{tot} will be negative in all glacial fjords. This term is associated with the difference in temperature between freshwater when it enters the fjord (at approximately the freezing temperature) and when it leaves the control volume in the mean barotropic component at θ_0 [Eq. (14)]. Since θ_0 will always be greater than the temperature of runoff or meltwater, this barotropic term will represent a divergence of heat and will thus be a negative component of the heat budget. In Sermilik, we have found that it is at least an order of magnitude smaller than other terms in the heat budget (Fig. 7). However, this will not be the case in all systems.

The ratio of H_0^{tot} to $H_{Melting}$ is

$$f_B = \frac{H_0^{tot}}{H_{Melting}}$$
$$= \frac{\rho c_p [Q_R(\theta_R - \theta_0) + Q_{MW}(\theta_{MW} - \theta_0)]}{\rho L_{adj} Q_{MW}}$$
$$= \frac{c_p}{L_{adj}} \left[\frac{Q_R}{Q_{MW}}(\theta_R - \theta_0) + (\theta_{MW} - \theta_0) \right]. \quad (25)$$

The magnitude of the barotropic fraction f_B increases as a function of Q_R/Q_{MW} and θ_0, as shown in Fig. 17. One can see that when $Q_R/Q_{MW} \sim O(1)$, as in Sermilik, H_0^{tot} will be an order of magnitude smaller than $H_{Melting}$. However, when $Q_R/Q_{MW} > 10$, H_0^{tot} becomes a similar magnitude as or larger than $H_{Melting}$.

(i) Neglecting the barotropic component

The studies of Motyka et al. (2013), Xu et al. (2013), Rignot et al. (2010), and Motyka et al. (2003) find ratios of Q_R/Q_{MW} (gray triangles in Fig. 17) between 2 and 31, such that the barotropic heat flux divergence would often be significant compared to the heat used for melting. If fjords fall in the part of parameter space that those papers claim ($Q_R \gg Q_{MW}$), the barotropic fluxes must not be ignored. Thus, their results indicate that their methods might be problematic because there is not an explicit separation of the unknown barotropic fluxes.

Sutherland and Straneo (2012), Johnson et al. (2011), and others remove the net transport through the fjord cross section, forcing the mass flux to zero and effectively dropping H_0^{tot} from the heat budget. This will produce errors on the melt-rate estimate as a function of Q_R/Q_{MW}, as shown in Fig. 17a. In the case of Petermann Fjord in Johnson et al. (2011), runoff should be small so neglecting H_0^{tot} should only create a ~5% error in the heat budget. Forcing the mass flux to zero and dropping H_0^{tot} will be inconsequential in fjords with low runoff, but it could create melt-rate errors of more than 150% in

fjords with $Q_R \gg Q_{MW}$. A more problematic approach than dropping H_0^{tot}, however, is including any barotropic fluxes without properly constraining the mass budget, as will be shown next.

(ii) Separating the barotropic components

Large errors can arise if the barotropic component of the cross-section velocity is not treated as an unknown. For example, consider a common equation for total heat transport in past literature: $H = c_p \rho \iint u(\theta - \theta_f) \, dA$. If the observed velocity contains some barotropic error u_0^{err}, which could be from instrument error, incomplete sampling coverage, tides, etc., then the error in the heat transport would be $H^{\text{err}} = c_p \rho u_0^{\text{err}}(\theta_0 - \theta_f) A_x$. For Sermilik Fjord values of $\theta_0 - \theta_f = 4.5°C$ and $A_x = 4.5 \times 10^6 \, \text{m}^2$, a barotropic velocity error of only $0.5 \, \text{cm s}^{-1}$ (a very small instrumental error or a small fraction of tidal velocities) would result in an enormous heat transport error of $3.7 \times 10^{11} \, \text{W}$, equivalent to $1000 \, \text{m}^3 \, \text{s}^{-1}$ of meltwater. If the barotropic velocity that balances the freshwater flux were measurable, a salt or heat budget would not be necessary to infer the total freshwater flux. Since this is not the case, the barotropic velocity should be separated and treated as an unknown.

2) STORAGE OF HEAT AND SALT

Sermilik connects to a shelf region with exceptionally strong wind forcing and high variability, resulting in large fjord velocities and heat/salt content variability. Similar shelf-forced flows are expected in other fjords of southeast Greenland with deep sills and an energetic adjacent shelf. Evidence of this has been found in Kangerdlugssuaq Fjord (Jackson et al. 2014). Fjords on the west coast (e.g., Gladish and Holland 2015; Mortensen et al. 2014), however, are found to have much weaker flows, and the fluctuating and storage terms should be reduced when shelf forcing (and the associated pycnocline heaving) is smaller. The question remains whether they would be small enough to neglect.

The potential importance of the storage term is explored with a simple scaling. If temperature variability in the control volume arises from pycnocline heaving, then an expression for H_{Storage} can be written using Eq. (21):

$$H_{\text{Storage}} = \rho c_p \left(\frac{\partial \langle \theta \rangle}{\partial t} \right) V_c = \rho c_p \left(\frac{\theta_U - \theta_L}{H} \right) \frac{\partial h}{\partial t} V_c, \qquad (26)$$

where $\langle \theta \rangle$ is the volume-averaged temperature; θ_U and θ_L are the average temperatures of the upper and lower layers, respectively; H is the total depth; and $\partial h / \partial t$ is the rate of vertical pycnocline displacements. The storage term increases with the amplitude of the pycnocline fluctuations, with the temperature difference between layers, and with the control volume size. To assess when this term can be neglected, it is scaled relative to the heat for melting to create a storage fraction ratio:

$$f_S = \frac{H_{\text{Storage}}}{H_{\text{Melting}}} = \frac{c_p(\theta_U - \theta_L)\frac{\partial h}{\partial t} WL}{L_{\text{adj}} Q_{MW}}, \qquad (27)$$

where we have approximated the control volume to be rectangular with a constant width W and length L (the distance from the cross section to the glacier).

Figure 17 shows the magnitude of the storage fraction, f_S from Eq. (27), as a function of the distance from the glacier and of pycnocline heaving, with fixed values of $\theta_U - \theta_L = -5°C$, $W = 7.5 \, \text{km}$, and $Q_{MW} = 400 \, \text{m}^3 \, \text{s}^{-1}$. One can see that our budgets for Sermilik Fjord are on the outer part of the shown parameter space, with measurements made far from the glacier ($L = 55 \, \text{km}$) and energetic pycnocline fluctuations ($\partial h / \partial t \approx 25$ or $13 \, \text{m day}^{-1}$ in winter and summer, respectively). With measurements at our mooring location, the error from neglecting the storage (without time averaging) would be equivalent to $\pm 3.6 \times 10^5 \, \text{m}^3 \, \text{s}^{-1}$ in summer and $\pm 6.4 \times 10^5 \, \text{m}^3 \, \text{s}^{-1}$ in winter—much larger than any plausible freshwater flux. In Sermilik, one would need ocean measurements within a few kilometers of the glacier, right in the mélange, for the storage term to be smaller than the heat for melting. This is not realistic with current technologies, so the storage terms must be assessed in budgets for Sermilik.

All previous studies have neglected the storage of heat and salt in their control volumes. The extent to which this is problematic depends on the fjord and the location of measurements: the storage terms are expected to be smaller in many previous studies of less energetic fjords with more accessible water near the glacier. Figure 17, however, shows that the instantaneous heat storage can still be large compared to melting even if pycnocline heaving is significantly smaller than in Sermilik or if measurements are made closer to the glacier. For the storage term to be small relative to the latent heat for $400 \, \text{m}^3 \, \text{s}^{-1}$ meltwater, measurements would need to be made within $O(100) \, \text{m}$ of the glacier and/or pycnocline fluctuations would need to be $O(1) \, \text{m day}^{-1}$. These are quite extreme conditions that might be met by some previous studies (e.g., Motyka et al. 2013, 2003) but certainly not all. The implication is that, in many cases, the heat storage term cannot be neglected; it must be evaluated directly or at least averaged in time to reduce its amplitude.

It should be noted that Eq. (26) will not always be a valid approximation for the storage term. For example,

when measurements are made very close to the glacier, within the convective plume region, it is likely that this scaling breaks down. Furthermore, measurements close to the glacier might be plagued by smaller scales of spatial variability as plumes emanate from the glacier (Stevens et al. 2015).

3) MEASURING A MEAN VELOCITY PROFILE

Almost all previous studies (except Mortensen et al. 2014) use short-term measurements of velocity or water properties to infer a quasi-steady exchange velocity, somewhat analogous to u_1. A variety of methods have been employed to extract a certain part of the velocity field. In some cases, the raw snapshots of velocity and water properties are used to calculate cross-section transport (Xu et al. 2013; Motyka et al. 2003, 2013; Rignot et al. 2010). In others, geostrophic velocities are calculated from water properties (Johnson et al. 2011; Inall et al. 2014) or a high-frequency mode is removed from the velocity field (Sutherland and Straneo 2012).

In Sermilik, we have found that measurements over at least several weeks are needed to separate an underlying exchange flow from the reversing synoptic-scale flows; the instantaneous velocity field, or even measurements over a week, are not sufficient for resolving u_1. Furthermore, it should be noted that both the u_1 profile in summer (Fig. 6) and the reversing shelf-forced flows of u_2 have a vertical structure that resembles the first baroclinic mode (Jackson et al. 2014). Therefore, any attempt to remove u_2 by fitting a first-mode structure to the observed velocity field could also remove a significant part of the u_1 signal. This could explain why the mean exchange velocity that we observe in summer is different, both in magnitude and structure, than the exchange velocity reported for Sermilik Fjord in Sutherland et al. (2014b) and Sutherland and Straneo (2012). This highlights the difficulty in disentangling a mean exchange flow from high-frequency flows without explicitly averaging in time, and we expect this problem to exist in many other systems.

4) THE IN SITU FREEZING POINT AND REFERENCE TEMPERATURES

While it is common practice to include a reference temperature in heat budgets, it should be noted that any particular choice of a reference temperature will not impact the total budget, nor one's ability to measure glacial fluxes from measurements of heat transport. The reference temperature will only change the relative magnitude of H_0, $\overline{H}_{MW}$, and $\overline{H}_R$, all of which are unknowns (section 2c). A reference temperature close to θ_{MW} and θ_R will reduce the amplitude of $\overline{H}_{MW}$ and $\overline{H}_R$ relative to H_0, but the sum of all three unknowns H_0^{tot} will not change.

Furthermore, a nonconstant reference temperature will distort the heat budget and lead to erroneous meltwater estimates. Many studies (e.g., Sutherland and Straneo 2012; Xu et al. 2013; Johnson et al. 2011) use a reference temperature of the in situ freezing temperature $\theta_f(S, P)$, which is a function of the local salinity and pressure, in an attempt to account for variability in the submarine meltwater temperature. However, a reference temperature can only be added to the heat budget if it is constant in space and time.

For example, in Sermilik and likely many other fjords, AW flows toward the glacier at depth, upwells when mixed with glacial inputs, and flows away from the glacier in an upper layer of glacially modified water. With an in situ freezing point reference temperature, the inflowing AW would be referenced to a colder temperature ($\theta_f \approx -2.2°C$ at 400 m) while the outflowing AW is referenced to a warmer temperature ($\theta_f \approx -1.8°C$ at 70 m). More generally, if any water mass transformations occur within the control volume that change the pressure and/or salinity of water masses, then a pressure- and salinity-dependent reference temperature of $\theta_f(S, P)$ will give erroneous results.

To quantify this, consider the exchange heat transport H_1 that is independent of a constant reference temperature (since $\int_{A_x} u_1 \, dA = 0$). The erroneous heat transport that would arise from measuring this transport with an in situ freezing point reference temperature would be $H_{1,err} = \rho c_p \int_{A_x} u_1(-\theta_f) \, dA$. If the exchange velocity is primarily a two-layer flow, like the summer conditions in Sermilik, then this expression can be simplified to $H_{1,err} = \rho c_p Q_1 \Delta\theta_f$, where Q_1 is the exchange volume flux from u_1 in each layer and $\Delta\theta_f$ is the difference between the average freezing temperature in the upper and lower layers. The error from using this in situ freezing temperature can be scaled relative to the heat used for melting as

$$\frac{H_{1,err}}{H_{Melting}} = \frac{c_p}{L_{adj}} \Delta\theta_f \frac{Q_1}{Q_{MW}}.$$

The error will increase as the exchange flow (Q_1) strengthens and as the freezing temperature diverges between the upper and lower layer (i.e., in deep fjords and fjords with strong vertical salinity gradients). In Sermilik during the summer, we find $Q_1 \approx 5 \times 10^4 \, m^3 \, s^{-1}$ and $Q_{MW} \approx 800 \, m^3 \, s^{-1}$, while $\Delta\theta_f = -(1.8–2.2)°C$. Therefore, if we used the in situ freezing point as a reference temperature, we would overestimate melting by 30%. This error might be significantly larger in fjords with more energetic exchange flows, for example, fjords with high runoff.

A preferable approach to account for variability in freezing point is to use a variable meltwater temperature

θ_{MW}. In Sermilik, the meltwater temperature could be $-2.0° \pm 0.4°C$ based on salinity of 30–35 and pressure of 0–630 db. This variability in θ_{MW} would change the multiplicative factor in Eq. (17) for Q_{MW} by only 0.5%; it would be insignificant. Accordingly, it is far better to have an error in the meltwater temperature (based on a range of in situ freezing temperatures) than a variable reference temperature.

6. Conclusions

We present complete mass, salt, and heat budgets for glacial fjords and new equations for inferring the freshwater fluxes of submarine melting and runoff. Building on the estuarine literature for salt budgets, this method includes a decomposition of the cross-section transports into barotropic, exchange, and fluctuating components—a decomposition that ensures mass conservation in the evaluated budgets and appropriately accounts for temporal variability. This method includes many terms that have been neglected in previous studies of submarine melting, and we highlight the importance of appropriately separating known versus unknown components of the advective transports.

We apply this method to Sermilik Fjord, a major glacial fjord into which Greenland's fifth-largest outlet, Helheim Glacier, drains. We assess the budgets for Sermilik Fjord using midfjord moorings that provide some of the most comprehensive and long-term measurements of velocity and water properties in a Greenlandic fjord to date. We find two different regimes seasonally that are consistent with the seasonal variations in fjord forcings: shelf variability via barrier winds and freshwater discharge from runoff.

During the nonsummer months (September–May), the fjord is dominated by shelf-forced flows that drive large variability in water properties. As a result, the leading-order heat and salt balances are between cross-section transports and changes in storage. During this period, the freshwater fluxes from the glacier cannot be inferred as a residual—they are indistinguishable from zero within the uncertainty of our estimates.

In the summer (May–August), the fluctuating velocity from shelf forcing is reduced and a clear structure emerges in the exchange velocity. The exchange flow consists of deep AW flowing toward the glacier and a thick upper layer flowing away from the glacier that is a mixture of AW and glacial inputs (meltwater and runoff). During this period, the total freshwater flux becomes distinguishable from zero and increases from June to August. The inferred submarine melting in August ($1500 \pm 500\,\mathrm{m}^3\,\mathrm{s}^{-1}$) is larger than most previous estimates of submarine melting and might contain significant iceberg meltwater. In the salt budget, the mean exchange imports salt and is primarily balanced by export from the barotropic transport. In the heat budget, the primary balance is between the import of heat from the exchange, the extraction of heat to melt ice, and changes in heat storage.

Beyond Sermilik, our methods and results have several important implications for inferring freshwater fluxes in other systems. The barotropic transports in fjords are typically not measurable but still important components of the budgets, requiring the use of both heat *and* salt budgets to accurately constrain the freshwater fluxes. The storage term will be important in most fjord budgets, unless a sufficiently long averaging time scale or small control volume is used. Temporal averaging is often necessary to resolve the mean exchange flow, which is found to be a dominant mode of heat/salt transport. Because of these and other findings, previous estimates of submarine melting are highly uncertain.

Ultimately, glacial fjord budgets are hard to evaluate for many reasons, including the presence of icebergs, the great depth of the fjords, and large temporal variability. In the future, more comprehensive mooring arrays, perhaps coupled with new methods for estimating submarine melting (e.g., from imaging of glacier fronts; Rignot et al. 2015; Fried et al. 2015), could provide a path forward for better constraining the freshwater fluxes. Additionally, icebergs might be a significant source of submarine melting in fjords, obscuring the glacier melt rate and requiring new methods to partition glacier and iceberg melting if glacier melt rates are to be estimated from oceanic measurements.

In previous studies of Greenlandic fjords, heat budgets are employed for the sole purpose of inferring melting. However, the evaluation of heat and salt budgets has value beyond that narrow goal by elucidating the dominant balances in the fjord, how heat/salt are transported, and how meltwater is exported. An improved understanding of fjord budgets is a necessary step toward understanding the oceanic controls on submarine melting and the ice sheet's impact on the ocean.

processing the data. Constructive and insightful comments from two anonymous reviewers are greatly appreciated.

APPENDIX A

Changes in Control Volume Size

Here, we explore the effect of changes in control volume size on the equations for inferring freshwater fluxes. If the full mass budget including control volume variability [Eq. (1)] is averaged in time, it can be written as

$$u_0 A_x + Q_{FW} = \frac{\partial V_c}{\partial t}. \tag{A1}$$

The time-averaged and decomposed salt budget, with V_c variability now included, is

$$u_0 S_0 A_x + F_1 + F_2 = \frac{\partial}{\partial t} \int_{V_c} S \, dV$$
$$= \frac{\partial \langle S \rangle}{\partial t} V_c + \frac{\partial V_c}{\partial t} \langle S \rangle, \tag{A2}$$

where $\langle S \rangle$ is the volume-averaged salinity such that $\langle S \rangle V_c = \int_{V_c} S \, dV$. Substituting the mass budget $u_0 A_x = (\partial V_c / \partial t) - \overline{Q_{FW}}$ into the salt budget gives

$$\left(\frac{\partial V_c}{\partial t} - Q_{FW} \right) S_0 + F_1 + F_2 = \frac{\partial \langle S \rangle}{\partial t} V_c + \frac{\partial V_c}{\partial t} \langle S \rangle. \tag{A3}$$

Solving for Q_{FW},

$$Q_{FW} = \frac{1}{S_0} (F_1 + F_2) - \frac{1}{S_0} \frac{\partial \langle S \rangle}{\partial t} V_c - \frac{1}{S_0} \frac{\partial V_c}{\partial t} \langle S \rangle + \frac{\partial V_c}{\partial t}$$
$$= \frac{1}{S_0} (F_1 + F_2) - \frac{1}{S_0} \frac{\partial \langle S \rangle}{\partial t} V_c + \left(1 - \frac{\langle S \rangle}{S_0} \right) \frac{\partial V_c}{\partial t},$$

where the last term on the right side is the only difference between this equation and Eq. (16) for Q_{FW} in which $\partial V_c / \partial t$ is neglected. The ratio of this neglected term ($Q_{FW,err}$, i.e., the error on our calculation) to the total freshwater flux is

$$\frac{Q_{FW,err}}{Q_{FW}} = \left(1 - \frac{\langle S \rangle}{S_0} \right) \frac{(\partial V_c / \partial t)}{Q_{FW}}. \tag{A4}$$

As shown in section 5a(2), we expect $(1 - \langle S \rangle / S_0) < 0.02$ for Sermilik. Thus, even if $\partial V_c / \partial t$ is an order of magnitude larger than Q_{FW}, the error in the freshwater equation will be small.

Similarly, the difference between the total equation for Q_{MW} that includes $\partial V_c / \partial t$ and the version that neglects it [Eq. (17)] can be scaled relative to the total meltwater flux:

$$\frac{Q_{MW,err}}{Q_{MW}} = \frac{T_0 - \langle T \rangle}{L_{adj}/c_p - (\theta_{MW} - \theta_R)} \frac{(\partial V/\partial t)}{Q_{MW}}, \tag{A5}$$

where $(T_0 - \langle T \rangle)/[L_{adj}/c_p - (\theta_{MW} - \theta_R)] < 0.01$ in Sermilik. Thus, we expect changes in V_c from the glacier terminus, icebergs, or sea level variability to have an insignificant effect on estimating freshwater fluxes with the heat and salt budgets.

APPENDIX B

Two-Layer Model for Shelf-Forced Flows

Here, a simple model for the shelf-forced flows (alternatively called intermediary circulation or baroclinic pumping) is used to explore the cross-fjord structure that is neglected in our analysis. We construct a two-layer model for a rectangular fjord where mass conservation and geostrophy are used to relate the upper-layer velocity to the pycnocline depth, the lower-layer velocity, and the cross-fjord pycnocline tilt. Following Arneborg (2004), we assume that the pycnocline heaving is approximately uniform throughout the fjord (see justification in section 4b), so that the upper-layer volume flux at any point is proportional to the rate of pycnocline displacement and the area upstream:

$$v_1 \overline{h} = \frac{\partial \overline{h}}{\partial t} L, \tag{B1}$$

where $\overline{h}$ is the spatially averaged depth of the pycnocline (positive with increasing depth), v_1 is the upper-layer velocity, and L is the length of the fjord upstream. By volume conservation, the volume flux in the lower layer must balance the upper layer:

$$v_1 \overline{h} = -v_2 (H - \overline{h}), \tag{B2}$$

where H is the total fjord depth and v_2 is the lower layer velocity. Then, based on thermal wind balance for a two-layer system, the cross-fjord pycnocline tilt will be

$$\frac{\partial h}{\partial x} = f(v_1 - v_2)/g', \tag{B3}$$

where $g' = \Delta\rho/\rho_0$ and $\Delta\rho$ is the density difference between layers. We expect the along-fjord velocity to be in geostrophic balance in Sermilik because the dominant time scale of fjord flows (3–10 days) is long compared to an inertial period (13 h) and the cross-fjord velocities are an order of magnitude smaller than the along-fjord velocities.

With these three governing equations, we impose a sinusoidal velocity in the upper layer, $v_1 = v_0 \sin(\omega t)$, so that the pycnocline depth can be solved from Eq. (B1) as
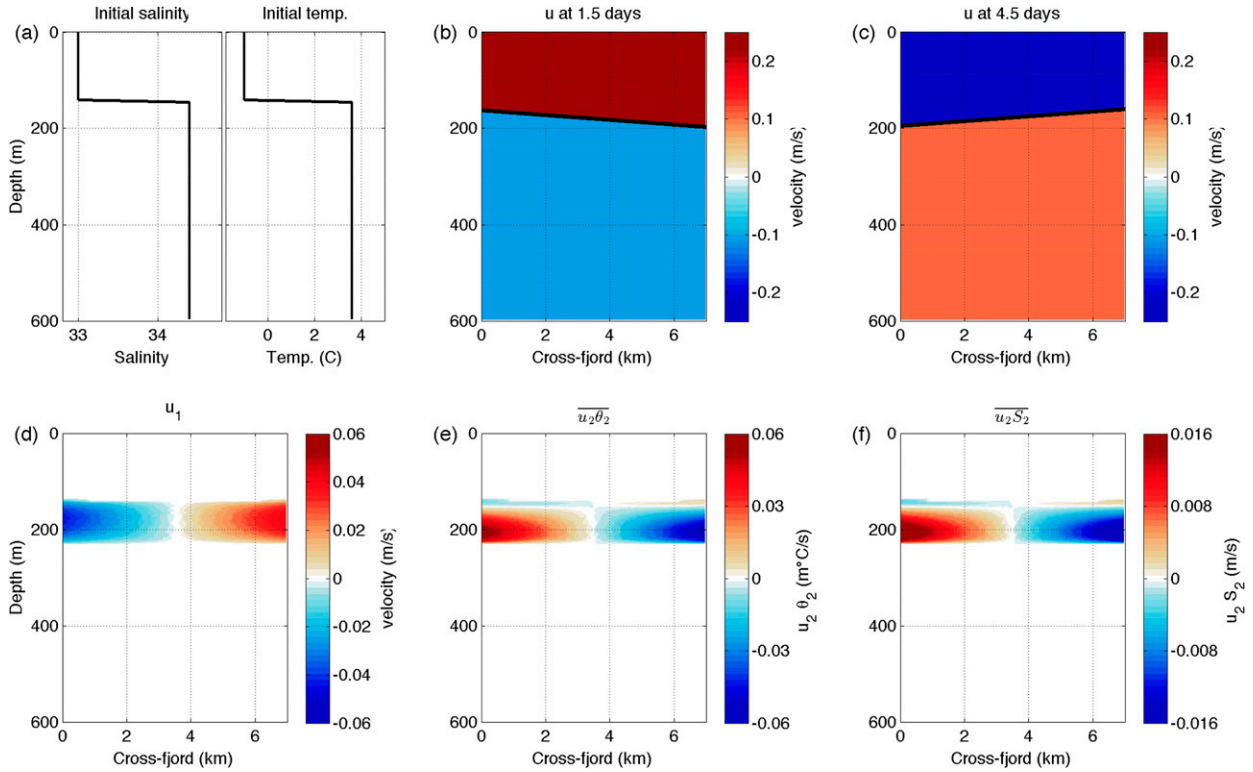
FIG. B1. Idealized two-layer model of shelf-forced flows. (a) Salinity and temperature vs depth for initial conditions. (b) Snapshot of velocity at 1.5 days (one-quarter of 6-day period) with interface shown in black. Mean interface is deepening, with its cross-fjord tilt in geostrophic balance with vertical shear. (c) Snapshot of velocity at 4.5 days (three-quarters of 6-day period) with interface shown in black. Mean interface is shoaling, with its cross-fjord tilt in geostrophic balance with vertical shear. (d) Time-averaged velocity $\overline{u} = u_1$ (since $u_0 = 0$) as a function of depth and cross-fjord distance. (e) Fluctuating transport of temperature $\overline{u_2\theta_2}$. (f) Fluctuating transport of salt $\overline{u_2S_2}$. Note that the cross-section averages of these three quantities (u_1, $\overline{u_2\theta_2}$, $\overline{u_2S_2}$) are zero; these plots highlight the biases that might arise from incomplete resolution of the fjord cross section.

$$\overline{h} = h_0 e^{-(v_0/L\omega)\cos(\omega t)}, \qquad (B4)$$

where h_0 is the time-averaged pycnocline depth. Since the fjord width (7 km) is less than the deformation radius (9 km) and we do not expect the pycnocline to outcrop, we make a final assumption that the pycnocline is linear across the fjord, such that its position is fully defined by the expressions for $\overline{h}$ and $\partial h/\partial x$.

We then assign the following values as representative for Sermilik Fjord in the nonsummer months: $v_0 = 0.3\,\mathrm{m\,s^{-1}}$, $\omega = 2\pi/6\,\mathrm{days^{-1}}$, $h_0 = 180\,\mathrm{m}$, $H = 600\,\mathrm{m}$, $L = 90\,\mathrm{km}$, and $g' = 9.5 \times 10^{-3}\,\mathrm{m\,s^{-2}}$. We construct a $600\,\mathrm{m} \times 7\,\mathrm{km}$ grid for a fjord cross section (with $5\,\mathrm{m} \times 50\,\mathrm{m}$ resolution) and evaluate the layer velocities and pycnocline location over 10 periods.

One simple thing that we find from this model is that, at the peak of the velocity pulses, the pycnocline depth varies by $\Delta h \sim 30\,\mathrm{m}$ across the 7-km-wide fjord. This is smaller than the mean vertical displacements (i.e., heaving) of 100 m but not negligible.

More importantly, the cross-fjord structure in this model has implications for our measurements of average velocity and fluctuating transports. In the model, there is no time-averaged volume flux in either layer; the layers expand and contract with pycnocline heaving, but there is no net transport. However, the mean velocity at every depth is not zero. Instead, in the depth range of pycnocline excursions, there will be a mean positive velocity (into the fjord) on the right side (looking upfjord) and a mean negative velocity on the left side (Fig. B1d). This could explain the mean inflow that we observe during both nonsummer periods (Figs. 6 and 13). Our moorings are off-center to the right/eastern side of the fjord, and the sign and magnitude of the observed mean flow at middepth are consistent with this model.

Similarly, while there is no net transport of heat and salt in either layer of this model, there are fluctuating transports of heat and salt (F_2 and H_2) in the depth range of pycnocline heaving, as shown in Figs. B1e and B1f. The sign and magnitude of these transports on the right side of the cross section are similar to our measurements

of H_2 and F_2 during the nonsummer months ([Fig. 15](#)). This model presents compelling evidence that part of the mean exchange flow and fluctuating transports that are measured during the nonsummer months in Sermilik could be partially or entirely an artifact of our limited cross-fjord coverage. During the summer, the shelf-forced pulses are significantly reduced and the mean exchange flow that we observe cannot be explained by this sampling bias.

APPENDIX C

Surface Fluxes

The surface heat fluxes are not directly evaluated, but their magnitude is estimated with the ERA-Interim reanalysis and local weather station data from the Sermilik region. A climatology of ERA-Interim in the coastal region outside Sermilik shows that in summer (May–August) the ocean typically gains $80 \, \mathrm{W \, m^{-2}}$, while in winter (December–March) there is a surface heat loss of $-100 \, \mathrm{W \, m^{-2}}$. These approximate values are corroborated by separate estimates of surface fluxes from weather station data in the Sermilik Fjord region, as reported in [Hasholt et al. (2004)](#). Net longwave and shortwave radiation are measured at the weather station, with a summer average of $+117 \, \mathrm{W \, m^{-2}}$ and a winter average of $-1 \, \mathrm{W \, m^{-2}}$. Sensible and latent heat fluxes are calculated with bulk formulas from measurements of wind speed, air temperature, relative humidity, and estimates of ocean surface temperature and speed, giving average sensible heat fluxes of $+2 \, \mathrm{W \, m^{-2}}$ in summer and $-42 \, \mathrm{W \, m^{-2}}$ in winter, and latent heat fluxes of $-3 \, \mathrm{W \, m^{-2}}$ in the summer and $-41 \, \mathrm{W \, m^{-2}}$ in the winter. These sum to an average total surface heat flux of $+84 \, \mathrm{W \, m^{-2}}$ in the summer and $-116 \, \mathrm{W \, m^{-2}}$ in the winter, similar to the ERA estimates.

When the ERA values are multiplied by the surface area of our control volume, the surface heat flux in Eq. [(11)](#) would have a magnitude of $-7.4 \times 10^{10} \, \mathrm{W}$ in winter and $+5.9 \times 10^{10} \, \mathrm{W}$ in summer. During the summer, these values are relatively small compared to our measurements of H_1 and H_{Storage}, which are both $O(10^{11}-10^{12}) \, \mathrm{W}$ ([Fig. 7](#)). Thus, during the summer, neglecting surface heat fluxes should not have a significant impact on our calculations of the freshwater fluxes. Neglecting this heat gain into the control volume means that we might underestimate submarine melting by $\sim 160 \, \mathrm{m^3 \, s^{-1}}$. In the winter, when the control volume loses heat to the atmosphere, we would overestimate submarine melting by $\sim 200 \, \mathrm{m^3}$, though we are not able to infer freshwater fluxes during the nonsummer months.

We have also neglected mass fluxes through the surface when simplifying the full mass budget for a glacial fjord [Eq. [(1)](#) reduced to Eq. [(6)](#)]. The mean annual precipitation from the nearby weather station is approximately $882 \, \mathrm{mm \, yr^{-1}}$ ([Hasholt et al. 2004](#)), which corresponds to a mass flux into the control volume of $22 \, \mathrm{m^3 \, s^{-1}}$. This is almost two orders of magnitude smaller than the inferred meltwater fluxes, so neglecting precipitation will not have an appreciable effect.

REFERENCES

Amundson, J. M., M. Fahnestock, M. Truffer, J. Brown, M. P. Lüthi, and R. Motyka, 2010: Ice mélange dynamics and implications for terminus stability, Jakobshavn Isbræ, Greenland. *J. Geophys. Res.*, **115**, F01005, doi:10.1029/2009JF001405.

Andersen, M. L., and Coauthors, 2010: Spatial and temporal melt variability at Helheim Glacier, East Greenland, and its effect on ice dynamics. *J. Geophys. Res.*, **115**, F04041, doi:10.1029/2010JF001760.

Andres, M., A. Silvano, F. Straneo, and D. R. Watts, 2015: Icebergs and sea ice detected with inverted echo sounders. *J. Atmos. Oceanic Technol.*, **32**, 1042–1057, doi:10.1175/JTECH-D-14-00161.1.

Arneborg, L., 2004: Turnover times for the water above sill level in Gullmar Fjord. *Cont. Shelf Res.*, **24**, 443–460, doi:10.1016/j.csr.2003.12.005.

Bamber, J., M. van den Broeke, J. Ettema, J. Lenaerts, and E. Rignot, 2012: Recent large increases in freshwater fluxes from Greenland into the North Atlantic. *Geophys. Res. Lett.*, **39**, L19501, doi:10.1029/2012GL052552.

Bartholomaus, T. C., C. F. Larsen, and S. O'Neel, 2013: Does calving matter? Evidence for significant submarine melt. *Earth Planet. Sci. Lett.*, **380**, 21–30, doi:10.1016/j.epsl.2013.08.014.

Beaird, N., F. Straneo, and W. Jenkins, 2015: Spreading of Greenland meltwaters in the ocean revealed by noble gases. *Geophys. Res. Lett.*, **42**, 7705–7713, doi:10.1002/2015GL065003.

Bendtsen, J., J. Mortensen, and K. Lennert, 2015: Heat sources for glacial ice melt in a West Greenland tidewater outlet glacier fjord: The role of subglacial freshwater discharge. *Geophys. Res. Lett.*, **42**, 4089–4095, doi:10.1002/2015GL063846.

Bevan, S. L., A. Luckman, S. A. Khan, and T. Murray, 2015: Seasonal dynamic thinning at Helheim Glacier. *Earth Planet. Sci. Lett.*, **415**, 47–53, doi:10.1016/j.epsl.2015.01.031.

Carroll, D., D. A. Sutherland, E. L. Shroyer, J. D. Nash, G. A. Catania, and L. A. Stearns, 2015: Modeling turbulent subglacial meltwater plumes: Implications for fjord-scale buoyancy-driven circulation. *J. Phys. Oceanogr.*, **45**, 2169–2185, doi:10.1175/JPO-D-15-0033.1.

Christoffersen, P., R. Mugford, K. Heywood, I. Joughin, J. Dowdeswell, J. Syvitski, A. Luckman, and T. Benham, 2011: Warming of waters in an East Greenland fjord prior to glacier retreat: mechanisms and connection to large-scale atmospheric conditions. *Cryosphere*, **5**, 701–714, doi:10.5194/tc-5-701-2011.

Chu, V. W., 2014: Greenland ice sheet hydrology: A review. *Prog. Phys. Geogr.*, **38**, 19–54, doi:10.1177/0309133313507075.

Enderlin, E. M., and I. M. Howat, 2013: Submarine melt rate estimates for floating termini of Greenland outlet glaciers (2000–2010). *J. Glaciol.*, **59**, 67–75, doi:10.3189/2013JoG12J049.

——, and G. Hamilton, 2014: Estimates of iceberg submarine melting from high-resolution digital elevation models: application to Sermilik Fjord, East Greenland. *J. Glaciol.*, **60**, 1084–1092, doi:10.3189/2014JoG14J085.

——, I. M. Howat, S. Jeong, M.-J. Noh, J. H. Van Angelen, and M. R. van den Broeke, 2014: An improved mass budget for the Greenland ice sheet. *Geophys. Res. Lett.*, **41**, 866–872, doi:10.1002/2013GL059010.

Farmer, D., and H. Freeland, 1983: The physical oceanography of fjords. *Prog. Oceanogr.*, **12**, 147–219, doi:10.1016/0079-6611(83)90004-6.

Foga, S., L. A. Stearns, and C. J. van der Veen, 2014: Application of satellite remote sensing techniques to quantify terminus and ice mélange behavior at Helheim Glacier, East Greenland. *Mar. Technol. Soc. J.*, **48**, 81–91, doi:10.4031/MTSJ.48.5.3.

Fried, M. J., G. A. Catania, and T. C. Bartholomaus, 2015: Distributed subglacial discharge drives significant submarine melt at a Greenland tidewater glacier. *Geophys. Res. Lett.*, **42**, 9328–9336, doi:10.1002/2015GL065806.

Gade, H., 1979: Melting of ice in sea water: A primitive model with application to the Antarctic ice shelf and icebergs. *J. Phys. Oceanogr.*, **9**, 189–198, doi:10.1175/1520-0485(1979)009<0189: MOIISW>2.0.CO;2.

Geyer, W. R., and D. K. Ralston, 2011: The dynamics of strongly stratified estuaries. *Water and Fine Sediment Circulation*, Vol. 2, *Treatise on Estuarine and Coastal Science*, R. J. Uncles and S. G. Monismith, Eds., Elsevier, 37–51, doi:10.1016/B978-0-12-374711-2.00206-0.

Gladish, C. V., and D. M. Holland, 2015: Oceanic boundary conditions for Jakobshavn Glacier. Part I: Variability and renewal of Ilulissat Icefjord waters, 2001–14. *J. Phys. Oceanogr.*, **45**, 3–32, doi:10.1175/JPO-D-14-0044.1.

Harden, B. E., I. A. Renfrew, and G. N. Petersen, 2011: A climatology of wintertime barrier winds off southeast Greenland. *J. Climate*, **24**, 4701–4717, doi:10.1175/2011JCLI4113.1.

——, F. Straneo, and D. Sutherland, 2014: Moored observations of synoptic and seasonal variability in the East Greenland coastal current. *J. Geophys. Res. Oceans*, **119**, 8838–8857, doi:10.1002/2014JC010134.

Hasholt, B., B. U. Hansen, O. Humlum, and S. H. Mernild, 2004: Meteorological stations at the Sermilik Station, Southeast Greenland: Physical environment and meteorological observations 2002. *Dan. J. Geogr.*, **104**, 47–58, doi:10.1080/00167223.2004.10649518.

Holland, D. M., R. H. Thomas, B. de Young, M. H. Ribergaard, and B. Lyberth, 2008: Acceleration of Jakobshavn Isbræ triggered by warm subsurface ocean waters. *Nat. Geosci.*, **1**, 659–664, doi:10.1038/ngeo316.

Howat, I. M., I. Joughin, and T. A. Scambos, 2007: Rapid changes in ice discharge from Greenland outlet glaciers. *Science*, **315**, 1559–1561, doi:10.1126/science.1138478.

Inall, M. E., T. Murray, F. R. Cottier, K. Scharrer, T. J. Boyd, K. J. Heywood, and S. L. Bevan, 2014: Oceanic heat delivery via Kangerdlugssuaq Fjord to the south-east Greenland ice sheet. *J. Geophys. Res. Oceans*, **119**, 631–645, doi:10.1002/2013JC009295.

Jackson, R. H., 2016: Dynamics of Greenland's glacial fjords. Ph.D. thesis, Massachusetts Institute of Technology /Woods Hole Oceanographic Institution, 172 pp., doi:10.1575/1912/7965.

——, F. Straneo, and D. A. Sutherland, 2014: Externally forced fluctuations in ocean temperature at Greenland glaciers in non-summer months. *Nat. Geosci.*, **7**, 503–508, doi:10.1038/ngeo2186.

Jenkins, A., 1999: The impact of melting ice on ocean waters. *J. Phys. Oceanogr.*, **29**, 2370–2381, doi:10.1175/1520-0485(1999)029<2370: TIOMIO>2.0.CO;2.

——, 2011: Convection-driven melting near the grounding lines of ice shelves and tidewater glaciers. *J. Phys. Oceanogr.*, **41**, 2279–2294, doi:10.1175/JPO-D-11-03.1.

Johnson, H. L., A. Münchow, K. K. Falkner, and H. Melling, 2011: Ocean circulation and properties in Petermann Fjord, Greenland. *J. Geophys. Res.*, **116**, C01003, doi:10.1029/2010JC006519.

Knudsen, M., 1900: Ein hydrographischer lehrsatz. *Ann. Hydrogr. Marit. Meteor.*, **28**, 316–320.

Lemke, P., and Coauthors, 2007: Observations: Changes in snow, ice and frozen ground. *Climate Change 2007: The Physical Science Basis*, S. Solomon et al., Eds., Cambridge University Press, 337–383.

Lerczak, J. A., W. R. Geyer, and R. Chant, 2006: Mechanisms driving the time-dependent salt flux in a partially stratified estuary. *J. Phys. Oceanogr.*, **36**, 2296–2311, doi:10.1175/JPO2959.1.

MacCready, P., and W. R. Geyer, 2010: Advances in estuarine physics. *Annu. Rev. Mar. Sci.*, **2**, 35–58, doi:10.1146/annurev-marine-120308-081015.

——, and N. S. Banas, 2011: Residual circulation, mixing, and dispersion. *Water and Fine Sediment Circulation*, Vol. 2, *Treatise on Estuarine and Coastal Science*, R. J. Uncles and S. G. Monismith, Eds., Elsevier, 75–89, doi:10.1016/B978-0-12-374711-2.00205-9.

Mernild, S. H., and Coauthors, 2010: Freshwater flux to Sermilik Fjord, SE Greenland. *Cryosphere*, **4**, 453–465, doi:10.5194/tc-4-453-2010.

Moffat, C., 2014: Wind-driven modulation of warm water supply to a proglacial fjord, Jorge Montt Glacier, Patagonia. *Geophys. Res. Lett.*, **41**, 3943–3950, doi:10.1002/2014GL060071.

Montgomery, R. B., 1974: Comments on "Seasonal variability of the Florida Current," by Niiler and Richardson. *J. Mar. Res.*, **32** (3), 533–535.

Moon, T., I. Joughin, B. Smith, M. R. Broeke, W. J. van de Berg, B. Noel, and M. Usher, 2014: Distinct patterns of seasonal Greenland glacier velocity. *Geophys. Res. Lett.*, **41**, 7209–7216, doi:10.1002/2014GL061836.

Mortensen, J., J. Bendtsen, K. Lennert, and S. Rysgaard, 2014: Seasonal variability of the circulation system in a west Greenland tidewater outlet glacier fjord, Godthåbsfjord (64 N). *J. Geophys. Res. Earth Surf.*, **119**, 2591–2603, doi:10.1002/2014JF003267.

Motyka, R., L. Hunter, K. Echelmeyer, and C. Connor, 2003: Submarine melting at the terminus of a temperate tidewater glacier, LeConte Glacier, Alaska, USA. *Ann. Glaciol.*, **36**, 57–65, doi:10.3189/172756403781816374.

——, W. P. Dryer, J. Amundson, M. Truffer, and M. Fahnestock, 2013: Rapid submarine melting driven by subglacial discharge, LeConte Glacier, Alaska. *Geophys. Res. Lett.*, **40**, 5153–5158, doi:10.1002/grl.51011.

Nick, F. M., A. Vieli, I. M. Howat, and I. Joughin, 2009: Large-scale changes in Greenland outlet glacier dynamics triggered at the terminus. *Nat. Geosci.*, **2**, 110–114, doi:10.1038/ngeo394.

——, and Coauthors, 2012: The response of Petermann Glacier, Greenland, to large calving events, and its future stability in the context of atmospheric and oceanic warming. *J. Glaciol.*, **58**, 229–239, doi:10.3189/2012JoG11J242.

Noel, B., W. J. van de Berg, E. van Meijgaard, P. Kuipers Munneke, R. S. W. van de Wal, and M. R. van den Broeke, 2015: Summer snowfall on the Greenland Ice Sheet: A study with the updated regional climate model RACMO2.3. *Cryosphere Discuss.*, **9**, 1177–1208, doi:10.5194/tcd-9-1177-2015.

Oltmanns, M., F. Straneo, G. W. K. Moore, and S. H. Mernild, 2014: Strong downslope wind events in Ammassalik, Southeast Greenland. *J. Climate*, **27**, 977–993, doi:10.1175/JCLI-D-13-00067.1.

Rignot, E., M. Koppes, and I. Velicogna, 2010: Rapid submarine melting of the calving faces of West Greenland glaciers. *Nat. Geosci.*, **3**, 187–191, doi:10.1038/ngeo765.

——, I. Fenty, Y. Xu, and C. Cai, 2015: Undercutting of marine-terminating glaciers in West Greenland. *Geophys. Res. Lett.*, **42**, 5909–5917, doi:10.1002/2015GL064236.

Schild, K. M., and G. S. Hamilton, 2013: Seasonal variations of outlet glacier terminus position in Greenland. *J. Glaciol.*, **59**, 759–770, doi:10.3189/2013JoG12J238.

Schjøth, F., C. S. Andresen, F. Straneo, T. Murray, K. Scharrer, and A. Korablev, 2012: Campaign to map the bathymetry of a major Greenland fjord. *Eos, Trans. Amer. Geophys. Union*, **93**, 141–142, doi:10.1029/2012EO140001.

Sciascia, R., F. Straneo, C. Cenedese, and P. Heimbach, 2013: Seasonal variability of submarine melt rate and circulation in an East Greenland fjord. *J. Geophys. Res. Oceans*, **118**, 2492–2506, doi:10.1002/jgrc.20142.

Shepherd, A., and Coauthors, 2012: A reconciled estimate of ice-sheet mass balance. *Science*, **338**, 1183–1189, doi:10.1126/science.1228102.

Stearns, L., and G. Hamilton, 2007: Rapid volume loss from two East Greenland outlet glaciers quantified using repeat stereo satellite imagery. *Geophys. Res. Lett.*, **34**, 5503–5508, doi:10.1029/2006GL028982.

Stevens, L. A., F. Straneo, S. B. Das, A. J. Plueddemann, A. L. Kukulya, and M. Morlighem, 2015: Linking catchment-scale subglacial discharge to subsurface glacially modified waters near the front of a marine terminating outlet glacier using an autonomous underwater vehicle. *Cryosphere Discuss.*, **9**, 4583–4624, doi:10.5194/tcd-9-4583-2015.

Stigebrandt, A., 2012: Hydrodynamics and circulation of fjords. *Encyclopedia of Lakes and Reservoirs*, L. Bengtsson, R. W. Herschy, and R. W. Fairbridge, Eds., Springer, 327–344, doi:10.1007/978-1-4020-4410-6_247.

Straneo, F., and P. Heimbach, 2013: North Atlantic warming and the retreat of Greenland's outlet glaciers. *Nature*, **504**, 36–43, doi:10.1038/nature12854.

——, and C. Cenedese, 2015: The dynamics of Greenland's glacial fjords and their role in climate. *Annu. Rev. Mar. Sci.*, **7**, 89–112, doi:10.1146/annurev-marine-010213-135133.

——, G. S. Hamilton, D. A. Sutherland, L. A. Stearns, F. Davidson, M. O. Hammill, G. B. Stenson, and A. Rosing-Asvid, 2010: Rapid circulation of warm subtropical waters in a major glacial fjord in East Greenland. *Nat. Geosci.*, **3**, 182–186, doi:10.1038/ngeo764.

——, R. G. Curry, D. A. Sutherland, G. S. Hamilton, C. Cenedese, K. Våge, and L. A. Stearns, 2011: Impact of fjord dynamics and glacial runoff on the circulation near Helheim Glacier. *Nat. Geosci.*, **4**, 322–327, doi:10.1038/ngeo1109.

Sutherland, D., and R. Pickart, 2008: The East Greenland coastal current: Structure, variability, and forcing. *Prog. Oceanogr.*, **78**, 58–77, doi:10.1016/j.pocean.2007.09.006.

Sutherland, D. A., and F. Straneo, 2012: Estimating ocean heat transports and submarine melt rates in Sermilik Fjord, Greenland, using lowered acoustic Doppler current profiler (LADCP) velocity profiles. *Ann. Glaciol.*, **53**, 50–58, doi:10.3189/2012AoG60A050.

——, ——, G. B. Stenson, F. J. M. Davidson, M. O. Hammill, and A. Rosing-Asvid, 2013: Atlantic water variability on the SE Greenland continental shelf and its relationship to SST and bathymetry. *J. Geophys. Res. Oceans*, **118**, 847–855, doi:10.1029/2012JC008354.

——, G. E. Roth, and G. Hamilton, 2014a: Quantifying flow regimes in a Greenland glacial fjord using iceberg drifters. *Geophys. Res. Lett.*, **41**, 8411–8420, doi:10.1002/2014GL062256.

——, F. Straneo, and R. S. Pickart, 2014b: Characteristics and dynamics of two major Greenland glacial fjords. *J. Geophys. Res. Oceans*, **119**, 3767–3791, doi:10.1002/2013JC009786.

Van As, D., and Coauthors, 2014: Increasing meltwater discharge from the Nuuk region of the Greenland ice sheet and implications for mass balance (1960–2012). *J. Glaciol.*, **60**, 314–322, doi:10.3189/2014JoG13J065.

van den Broeke, M., and Coauthors, 2009: Partitioning recent Greenland mass loss. *Science*, **326**, 984–986, doi:10.1126/science.1178176.

Xu, Y., E. Rignot, D. Menemenlis, and M. Koppes, 2012: Numerical experiments on subaqueous melting of Greenland tidewater glaciers in response to ocean warming and enhanced subglacial discharge. *Ann. Glaciol.*, **53**, 229–234, doi:10.3189/2012AoG60A139.

——, ——, I. Fenty, D. Menemenlis, and M. Mar Flexas, 2013: Subaqueous melting of Store Glacier, West Greenland from three-dimensional, high-resolution numerical modeling and ocean observations. *Geophys. Res. Lett.*, **40**, 4648–4653, doi:10.1002/grl.50825.